Shock-darkening in ordinary chondrites
Mesoscale modelling of the shock process and comparison with shock-recovery experiments

JUULIA-GABRIELLE MOREAU

ACADEMIC DISSERTATION
To be presented, with the permission of the Faculty of Science of the University of Helsinki, for public examination in auditorium E204, Physicum, Kumpula Campus, on 5th of April 2019, at 12 o' clock noon.

DEPARTMENT OF GEOSCIENCES AND GEOGRAPHY A71 / HELSINKI 2019

© Juulia-Gabrielle Moreau (synopsis)
© Reprinted with the permission of Wiley (Paper I)
© Reprinted with CC BY license of Open Access Articles (Paper II; Paper III submitted)
Cover photo: shock-darkening in the Chelyabinsk meteorite (Tomas Kohout)
Back cover photo: © Helene K. Studio Photography (resized)

Author´s address: Juulia-Gabrielle Moreau
Department of Geosciences and Geography
P.O.Box 64
00014 University of Helsinki, Finland
juulia.moreau@helsinki.fi

Supervised by: Dr. Tomas Kohout
Department of Geosciences and Geography
University of Helsinki;
Institute of Geology, The Czech Academy of Sciences
Czech Republic

Prof. Ilmo Kukkonen
Department of Geosciences and Geography
University of Helsinki

Co-supervised by: Prof. Kai Wünnemann
Museum für Naturkunde
Leibniz Institute for Evolution and Biodiversity Sciences
Germany

Reviewed by: Prof. Falko Langenhorst
Analytische Mineralogie der Mikro- und Nanostrukturen
Institut für Geowissenschaften
Germany

Dr. Thomas M. Davison
Department of Earth Science & Engineering
Imperial College, London
United Kingdom

Opponent: Prof. Thomas Sharp
School of Earth and Space Exploration
Arizona State University
United States of America

ISSN-L 1798-7911
ISSN 1798-7911 (print)
ISBN 978-951-51-3995-5 (paperback)
ISBN 978-951-51-3996-2 (PDF)
http://ethesis.helsinki.fi

Unigrafia
Helsinki 2019

The Faculty of Science uses the Urkund system (plagiarism recognition) to examine all doctoral dissertations.

"Light thinks it travels faster than anything but it is wrong.
No matter how fast light travels, it finds the darkness
has always got there first, and is waiting for it."
(Reaper Man, Terry Pratchett)

Moreau J., 2019. *Shock-darkening in ordinary chondrites: mesoscale modelling of the shock process and comparison with shock-recovery experiments*. Unigrafia. Helsinki. 60 pages, 6 tables and 21 figures.

Abstract

Ordinary chondrites are primitive materials of the solar system; they were subject to thermal and shock metamorphism during asteroid accretion and collision history.

Shock-darkening is a shock metamorphic process which occurs in ordinary chondrites where iron sulphides and metals form a network of tiny melt veins, optically darkening the lithology. Together space weathering and shock-darkening can be a major factor in alteration of reflectance spectra, suppressing the 1 and 2 micron silicate absorption bands. S-complex asteroids, hosting ordinary chondrites, display silicate absorption bands. C/X-complex asteroids are either devoid of 1 and 2 micron silicate absorption bands or presenting a weak silicate absorption band at 1 micron. If shock-darkening can alter the spectra of S-complex asteroids, they can appear like C/X-complex asteroids and induce a mismatch in the asteroid distribution.

This thesis provides an in-depth study of shock-darkening in order to determine the pressure-temperature conditions for shock melting of both iron sulphides and metals, in ordinary chondrites. In order to perform this study the following actions were required:

I. observing shock wave interactions in heterogeneous mediums composed of silicates, metals, and iron sulphides, the principal components of ordinary chondrites

II. quantifying post-shock heating and melting of the individual phases

III. comparing my results with observations of shock metamorphism in ordinary chondrites

IV. investigating on the best conditions to reproduce shock-darkening in shock-recovery experiments.

In contrast to shock-recovery experiments, I adopted a numerical modelling method which calculated the post-shock heating and melting of individual phases and provided observation of shock wave interactions in heterogeneous mediums. The shock physics code iSALE was used on a mesoscale to study shock compression of ordinary chondrites. Using complex models, the numerical study lead to the following results:

A) 40−60 GPa is the likely range for shock-darkening, dominated by melting of iron sulphides.

B) Heterogeneous distribution of peak shock pressures and post-shock heating is caused by strong impedance contrasts between phases (with strong pressure increases through reflections from high density phases to lower density phases, e.g. metals to silicates).

C) Special conditions, such as eutectic melting, hotspots from convergence of shock waves, or pore crushing, are necessary to melt metals.

D) Porosity and pre-heating are important boundary conditions affecting shock metamorphism.

E) Results from the mesoscale models are compatible to observations of shock metamorphism in ordinary chondrites.

Finally, simulations of shock-recovery experiments showed that the reverberation technique may prevent shock-darkening from occurring. Compared to a single pressure load, the reverberation technique reduces the rise in entropy from super-imposing pressures, thus, if sufficient pressure for shock-darkening (40–60 GPa) is achieved, melting of iron sulphides or metals may not occur. Alternatively, I showed that spherical shock-recovery experiments, which use spherically induced shock waves to shock spherical samples, are ideal to study shock-darkening because the rise in entropy is directly related to the peak-shock pressure in the sample.

With my results, a more in depth quantitative study of the volume of shock-induced darkened materials during asteroid collisions is now possible.

Résumé (in French)

Les chondrites ordinaires sont des roches primitives du système solaire sujettes au métamorphisme thermique et de choc survenant sur les astéroïdes.

Le noircissement par choc dans les chondrites ordinaires est un processus exclusif au métamorphisme de choc. Par fusion, les sulfures de fer et de métaux forment un réseau de minuscules veines qui noircissent la lithologie. Avec la météorologie spatiale, le noircissement par choc est un facteur majeur dans l'altération des spectres de réflexion puisqu'il élimine les bandes d'absorption à 1 et 2 microns des composés silicatés. Les spectres des astéroïdes du groupe S (intégrant les chondrites ordinaires) possèdent ces bandes d'absorption, là où ceux des astéroïdes du groupe C/X en sont dénués ou possèdent une faible absorption à 1 micron. Si le noircissement par choc altère les spectres des astéroïdes du groupe S, ceux-ci peuvent ressembler à ceux du groupe C/X et occasionner une incohérence dans la distribution des astéroïdes.

Dans ma thèse, j'ai étudié le noircissement par choc en déterminant les conditions de pression et température nécessaires à la fusion des sulfures de fer et métaux dans les chondrites ordinaires. Plus précisément, j'ai eu besoin de :

I. observer les interactions d'ondes de choc dans des milieux hétérogènes composés de silicates, métaux et sulfures de fer, principales phases minérales des chondrites ordinaires

II. quantifier les températures post-choc et la fusion de ces phases minérales

III. comparer mes résultats avec la littérature sur le métamorphisme de choc dans les chondrites ordinaires

IV. explorer les conditions idéales pour reproduire le noircissement par choc dans des expériences de récupération (de choc).

Au détriment des expériences de récupération, j'ai opté pour la modélisation numérique afin de quantifier les températures post-choc et la fusion des différentes phases minérales, et observer in situ les interactions d'onde de choc dans un milieu hétérogène. Par l'usage d'un code de physique des chocs (iSALE), j'ai mené cette étude sur les chondrites ordinaires. Profitant de modèles complexes, les résultats obtenus sont les suivants :

A) Le noircissement par choc, dominé par la fusion des sulfures de fer, se produirait aux pressions de 40–60 GPa.

B) Les forts contrastes d'impédance entre phases (e.g. entre métaux et silicates) provoquent une distribution hétérogène des pics de pression et de température post-choc causés par des réflexions de choc.

C) La fusion eutectique et les zones de hautes températures (provoquées par la convergence d'ondes de choc ou la fermeture de pores) sont des conditions nécessaires pour la fonte des métaux.

D) La porosité initiale et le métamorphisme thermique sont d'autres conditions ayant un effet sur le métamorphisme de choc.

E) Les résultats inhérents aux modèles numériques sont en accord avec la littérature sur le métamorphisme de choc dans les chondrites ordinaires.

Finalement, des modèles numériques sur les expériences de récupération montrent que la technique de réverbération est limitée pour le noircissement par choc. Contrairement à une hausse instantanée de pression, la réverbération réduit l'entropie en accumulant les pressions. Ainsi, si la pression requise pour le noircissement par choc est atteinte (40–60 GPa), la fusion des sulfures de fer ou des métaux peut ne pas se produire. Cependant, j'ai démontré que les expériences de récupération qui profitent d'ondes de choc sphériques sont idéales pour produire le noircissement par choc. En effet, dans ces expériences, l'entropie correspond à la pression atteinte dans l'échantillon.

Avec mes résultats, une étude sur la quantification du volume de matériaux soumis au noircissement par choc pendant les collisions entre astéroïdes est désormais envisageable.

Acknowledgements

First, and most important, I am indebted to my supervisor, Dr. Tomas Kohout.

Without Tomas, I would not be presenting my thesis today. He helped me set my research in motion, introduced me to the Planetary Science community through conferences and research visits. Writing my research output benefited from his precious help, advice, and his unyielding support throughout my Ph.D. thesis. He always supported my ideas and helped me to boost up my confidence by presenting my research to the scientific community. He always offered me new challenges to tackle.

"Life is hard" (Tomas Kohout)

Second, I will never forget the constructive feedback from my German supervisor, Prof. Kai Wünnemann.

My enjoyable visits at the Museum für Naturkunde in Berlin was successful as he welcomed me to his team with conviviality and was always available to share his knowledge with me. He was keen to support my ideas, but always ensured I was not overrating my research with impossible hopes.

"Make it simpler" (Kai Wünnemann)

I am also thankful to my professor supervisor, Ilmo Kukkonen.

He had the arduous task of monitoring my research in the midst of my doctoral studies. His consulting and assistance supports always put me back on track and allowed me to understand were I stood.

And many thanks to my Ph.D. thesis pre-examiners, Prof. Dr. Falko Langenhorst and Dr. Thomas (Tom) Davison, for their thoughtful comments on my thesis synopsis and their suggestions for improvement.

To the scientific community of the University of Helsinki:

- Johanna Salminen who supported me at the dawn of my teaching duties and studies;
- Kateřina, Robert, Janina, Henrik—and others—, my valuable colleagues of that time; and all professors that taught me at the University of Helsinki.
- I bestow my utmost gratitude upon Anu Kaakinen who, many years ago, introduced me to the University of Helsinki and never ever complained about my betrayal of changing from sedimentology.
- My thanks go also to Radek and Stefan for helping me to produce BSE and optical microscope images of meteorite thin sections for the synopsis.
- And I do not forget David Whipp who allowed me to help improving diversity, inclusivity, and well-being, in our community.

To all my colleagues from the Planetary Science community, the Museum für Naturkunde, the iSALE team and developers, Gareth Collins, Kai Wünnemann, Dirk Elbeshausen, Boris Ivanov, and Jay Melosh.

Special thanks to Tom Davison for the pySALEPlot tool used by iSALE users.

To Robert Bouchier and Johnnie Lester for their last-minute English appraisal and editing of the synopsis.

To my family, my mother Isabelle, my father Jacques, my brother Vincent, and everyone else.

To my best friend Florence and esteemed friends Irina, Salla, Annick, and others.

To Laura, my little soul sister.

To my mentor, Prof. Alain Préat, who introduced me to the wonders of geology.

And finally, to the strong support I received from everyone when I faced important changes in my life that affected my Ph.D. project from without and within.

Juulia-Gabrielle Moreau

Contents

List of original publications

This thesis is based on the following publications:

I. Moreau J., Kohout T., and Wünnemann K. 2017. Shock-darkening in ordinary chondrites: determination of the pressure-temperature conditions by shock physics mesoscale modeling. *Meteoritics & Planetary Science*, 52(11):2375–2390, doi:10.1111/maps.12935.

II. Moreau J., Kohout T., and Wünnemann K. 2018a. Melting efficiency of troilite–iron assemblages in shock-darkening: insight from numerical modeling. *Physics of the Earth and Planetary Interiors*, 282:25–38, doi:10.1016/j.pepi.2018.06.006.

III. Moreau J., Kohout T., Wünnemann K., Halodova P., and Haloda J. 2018b. Shock physics mesoscale modeling of shock stage 5 and 6 in ordinary and enstatite chondrites. *Icarus*, submitted.

The publications are referred to in the text by their Roman numerals

Author's contribution to the publications

I. All models, methods, results, discussion, figures and tables.

Co-authors: T. Kohout provided the study with the idea of a systematic modelling of H, L and LL chondrites, and with the most important questions that needed to be answered. K. Wünnemann provided follow-up on the models set-up, and analysis, and the principles of iSALE modelling. Both co-authors improved the manuscript interpretations, illustrations, and scientific writing.

II. All models, methods, results, discussion, figures and tables.

Co-authors: T. Kohout provided BSE images to illustrate the iSALE model configurations and how to best represent the general results of the study. T. Kohout and K. Wünnemann provided the study with ideas for additional models and illustrations, and improvement of manuscript interpretations and scientific writing.

III. All models, methods, results, discussion, figures and tables.

Co-authors: T. Kohout proposed a more in-depth study of shock metamorphism and comparison with the shock classification and how to best interpret the results. P. Halodova and J. Haloda provided the back-scattered electron microscope images. All co-authors improved the manuscript interpretations, illustrations, and scientific writing.

Additional results for shock-recovery experiments, impact modelling, and observations on optical and scanning electron microscopes are provided within the thesis.

Abbreviations

OC(s)	**O**rdinary **c**hondrite(s)
M(A)B	**M**ain (**A**steroid) **B**elt
AU	**A**stronomical **U**nit
EoS	**E**quations **o**f **s**tate
LL	Very **l**ow in iron
L	**L**ow in iron
H	**H**igh in iron
C-S*n*	**S**hock stage *n* (in **c**hondrites)
ANEOS	**An**alytical **e**quations **o**f **s**tate
BSE	**B**ack-**s**cattered **e**lectron
CPPR	**C**ells **p**er **p**rojectile **r**adius

List of tables and figures

1 Introduction

1.1 Origin of the project

On the 15th of February 2013, at 9.22 am, in the Chelyabinsk region, Russia, an asteroid penetrated the Earth's atmosphere and blasted into pieces (Fig. 1). The atmospheric disruption generated a shock wave shattering windows and injuring many. The fireball was witnessed by thousands and hit the news worldwide. "*Pluie de Météorites en Russie*" wrote the Belgian news, *Le Soir*, when I checked the news from my computer, working hard on some chemical experiment in Brussels. Hence, the meteorite fall was thoroughly studied by scientists (e.g. Kohout et al. 2014 and references within, Righter et al. 2015). The fallen meteorites were identified as ordinary chondrites (OCs).

The Chelyabinsk meteorites displayed the following lithologies:

- a light lithology with mineralogy and geochemical composition of LL chondrites
- a dark lithology with mineralogy and geochemical composition similar to the light lithology
- a dark impact melt lithology where silicates are extensively molten.

These lithologies are composition of a genomict breccia (Bischoff et al. 2006) and constrain the parent body evolution. In the progressive shock metamorphism classification (Stöffler et al. 1991, 2018), the light lithology is of shock stage 4 (C-S4), whereas the dark lithology is of unknown shock stage.

The darkening observed in the dark lithology is called shock-darkening. Shock-darkening is a shock metamorphic process in which iron sulphide and metal melt veins spread into silicate cracks (Heymann 1967); it darkens the lithology which is, thereafter, optically opaque. In Kohout et al. (2014), they carried out extra tests using

Fig. 1. The dust cloud of the Chelyabinsk meteorite fall. The thickest part is the major blast zone. Photo credits: Alex Alishevskikh. Source: https://www.nasa.gov/feature/five-years-after-the-chelyabinsk-meteor-nasa-leads-efforts-in-planetary-defense (28th February 2018).

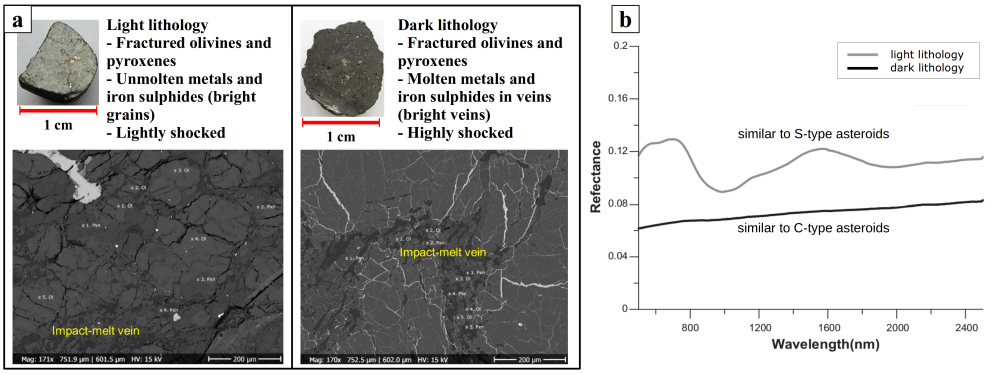

Fig. 2. Comparison between the light and shock-darkened lithologies of Chelyabinsk LL5 meteorite with a) samples and BSE images and b) reflectance spectra. Modified from Kohout et al. (2014).

analysis of reflectance spectra. The spectra of the light lithology and the shock-darkened lithology are dissimilar (see Fig. 2). The light lithology spectrum shows two silicate absorption bands at 1 and 2 microns. In the shock-darkened lithology, these silicate absorption bands are absent. Shock-darkening is a different process to that of space weathering which can also darken the asteroid surfaces. For example, the irradiation of solar wind can lead to the formation of nanoparticulate iron which reddens or darkens the reflectance spectra of asteroids (Clark et al. 2002).

The asteroid classification is based on reflectance spectra of asteroids (DeMeo et al. 2009, DeMeo and Carry 2014). For example S-complex asteroids have reflectance spectra showing two silicate absorption bands at 1 and 2 microns and they host OCs. C/X-complex asteroids have spectra either devoid of 1 and 2 micron silicate absorption bands or presenting a weak silicate absorption band at 1 micron (possibly having a hydrated silicate absorption band at 0.7 micron). According to their reflectance spectra, composition of C/X-complex asteroids is different from S-complex asteroids. By extension, the light lithology spectra of the Chelyabinsk meteorite are similar to S-complex asteroids and the shock-darkened lithology spectra of the Chelyabinsk meteorite are similar to C/X-complex asteroids. However, the two lithologies do not differ in composition like S- and C/X-complex asteroids do. If shock-darkening can alter S-complex asteroid spectra, then a mismatch in the distribution between S- and C/X-complex asteroids exists on condition that shock-darkened material is exposed or ejected during asteroid collisions.

This observation raises the question: *How many asteroids classified as C/X-complex asteroids are, indeed, shock-darkened S-complex asteroids?* Answering this question would also deliver a better understanding of the asteroid classification and reassess it.

1.2 Research questions and methodology

My thesis aims particularly for a better understanding of shock-darkening in OCs and estimation of the conditions for this process to occur. Because shock-darkening is a shock metamorphic process, several questions must be answered and they are:

I. What temperature and pressure conditions are required for the melting and spreading of iron sulphides and metals into the silicate cracks?
II. What is the proportion of iron sulphide melt to metal melt and what conditions are required for the abundance of melt? In literature, there is no evidence of which phase is dominant in the shock-darkening veins.

III. How can thermal metamorphism and porosity influence shock-darkening? The shock classification is based on pressure and post-shock temperature estimates in olivine. Thus, it is interesting to know how these two parameters affect shock metamorphism in general.

IV. Can we reproduce shock-darkening in shock-recovery experiments at the estimated pressure conditions? Benchmarking numerical results with experiments to reproduce shock effects is key to scientific research.

V. Are reverberation techniques in experiments (e.g. Langenhorst and Deutsch 1994, Langenhorst and Hornemann 2005) better than spherical shocks (e.g. Bezaeva et al. 2010) to reproduce shock-darkening?

VI. Assuming from question I, what is the volume of shock-darkened material produced in asteroid collisions and is shock-darkened material ejected and exposed upon impact? Because shock-darkening alters reflectance spectra, the material must be exposed to hold significance for the observation and distribution of asteroids.

To answer questions I to V, it is required to:

A) understand the shock wave interactions in heterogeneous materials similar to OCs (e.g. silicate, metal and iron sulphide phases)

B) quantify post-shock heating and melting of the individual phases and how pressure impedance contrasts of different phases affect the distribution of post-shock temperatures—in contrast to thermal metamorphism where phases heat homogeneously

C) benchmark results with observations of shock metamorphism and the shock classification of OCs (Stöffler et al. 1991, 2018)

D) optimize the experimental set-up in shock-recovery experiments and try to understand how shock heating, or progressive shock metamorphism, occurs in reverberation or spherical shock-recovery experiments.

Shock-recovery experiments are ideal to observe the outcomes of shock loading on rock samples. However, shock-recovery experiments are restricted for observing shock wave interactions in heterogeneous mediums and they lack the possibility to quantify post-shock heating of phases. This is why numerical modelling was used to study shock compression of heterogeneous mediums similar to OCs; the shock physics code iSALE (Wünnemann et al. 2006) was chosen accordingly. Furthermore, I simulated shock-recovery experiments using the reverberation technique and spherical shocks to understand how such experiments work and how reliable they are to study progressive shock metamorphism. I also conducted preliminary models to quantify the production of shock-darkened materials in asteroid collisions.

1.3 Asteroids and meteorites

Meteorites are extraterrestrial rocks that survived atmospheric entry (Norton 2002) and impact cratering on Earth's surface. They are remnants of asteroids, one major component of the solar system. Upon entry to Earth, meteorites are either classified as *finds* or *falls*. A find undergoes weathering on the surface of the Earth, unless it landed in very dry or cold regions (e.g. deserts, Antarctica) for short periods of time. A fall is less affected by meteorological weathering because such meteorites are soon recovered; unless otherwise, the trajectory of the fireball and landing site are estimated to help recover the meteorites.

All data on meteorite falls and finds are archived in an international database, the *Meteoritical Bulletin Database* managed by *The Meteoritical Society*. Amongst falls and finds, OCs are the most abundant, followed by achondrites and carbonaceous chondrites.

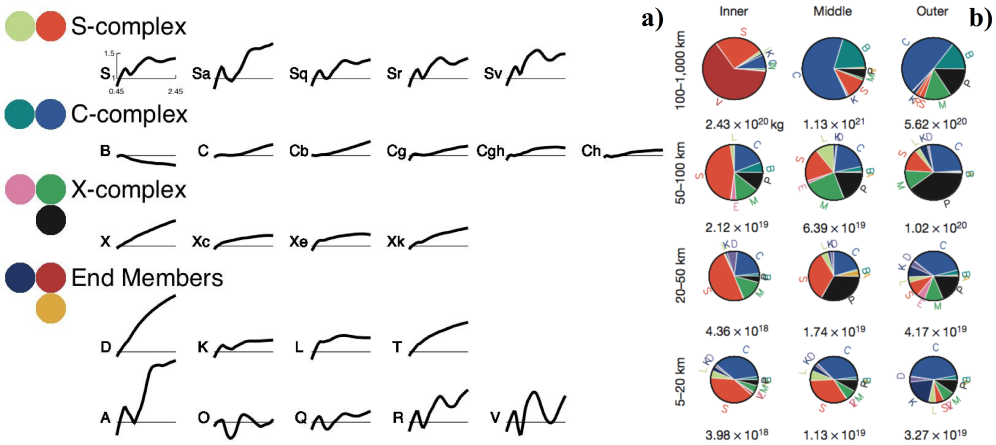

Fig. 3. a) Reflectance spectra Bus-DeMeo taxonomy key for the MAB and b) the corresponding distribution in the Inner, Middle, and Outer Main Belt (adapted from DeMeo et al. 2009, DeMeo and Carry 2014). The colour markers in a) were added to the taxonomy key to correspond to the colour scheme in b). The sizes in km are the diameter ranges for the asteroids.

Link to the *Meteoritical Bulletin Database*: https://www.lpi.usra.edu/meteor/metbull.php

1.3.1 Asteroidal origin of meteorites

At the origin of the solar system when the primordial Sun was surrounded by a disc of dust and gas, dynamics processes, condensation, and recrystallization, lead to the formation of planetary bodies and asteroids (Bottke et al. 2002, Lauretta and McSween 2006, Michel et al. 2015). Accretion and disruption of planetesimal bodies progressively formed the major planets, dwarf planets, and asteroid regions. To name a few, asteroid regions are, up to 5.2 AU:

- the Near Earth Asteroids (NEA) or Near Earth Objects (NEO)—these asteroids are mostly objects ejected from the MAB (e.g. impacts, Kirkwood gaps, resonance motion with other planetary bodies), or other regions, and they possess their own orbits which can cross the Earth orbit and pose a risk to collide with Earth
- the MB asteroids in the 2–3 AU region, where most of collected meteorites originate from —the MAB is divided in three major regions: the inner (2.1–2.5 AU), middle (2.5–2.8 AU), and outer (2.8–3.5 AU) regions; the distribution and dynamic evolution of asteroids in the MB are well known (DeMeo et al. 2009, DeMeo and Carry 2014, Morbidelli et al. 2015) and use reflectance spectra of asteroids in the near-infrared (see section 1.3.2)
- the Jovian Trojan asteroids—they are in the same orbital as Jupiter (5.2 AU).

1.3.2 Classification of asteroids and evolution of the Main Asteroid Belt

To identify small bodies in the solar system and classify them, spectral observations are used. The taxonomy of asteroids is based on the visible and near-infrared spectral features. DeMeo et al. (2009) describe the techniques to classify asteroids. One technique is to identify features present in the spectra such as: the slope, the shape, depth, and width of spectral gaps at the 1 and 2 micron bands (silicates). They determined 24 classes with two major groups of spectra: those with distinct features in the 1 and 2 micron absorption bands, and those devoid of such features. An overview of the different classes and the spectral types are shown in Fig. 3a, showing 4 categories:

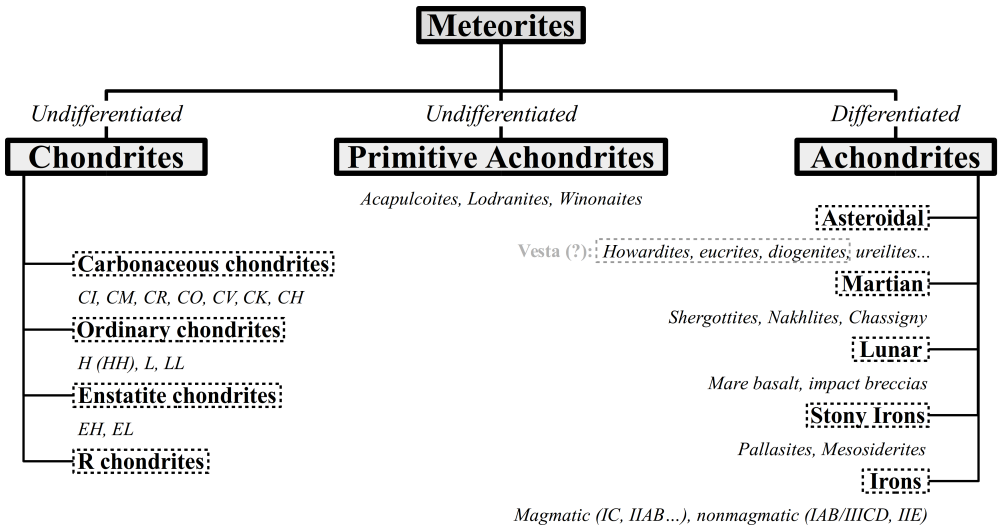

Fig. 4. Meteorite classification (simplified from Rubin 1997 and Weisberg et al. 2006).

- the C-complex asteroids, with low albedo and flat slopes, mostly featureless, hosting carbonaceous chondrites
- the S-complex asteroids with distinct silicate absorption features, hosting OCs
- the X-complex asteroids with moderate slopes and mostly featureless, often iron-rich objects or carbonaceous chondrites
- end-member asteroids, less common with more distinct features (e.g. D-types asteroids with red-sloped spectra or Q-types asteroids with spectra similar to LL OCs).

The classification for the MAB is ideal to understand the evolution of the solar system. In DeMeo and Carry (2014) they illustrate the mixing of asteroids in the MB (see Fig. 3b, current distribution of asteroids in the Inner, Middle, and Outer MB). The two major hypotheses to explain the mixing of asteroids in the solar system and the MAB are the Nice and Grand Tack models. Both models hypothesize the migration of gas giants in the solar system. The Nice model explains mixing of asteroids through the migration (change in orbits) of giant planets between ~800 My and ~1000 My after the formation of the solar system, on short scale (AU). The Grand Tack model (<600 ky) focuses on the strong migration of giant gas planets (e.g. Jupiter migrating to the current orbit of Mars) and the mixing of asteroids formed nearby the Sun and asteroids formed farther in the system (e.g. >10 AU). Such disturbances allowed asteroids of different regions to coexist in today's regions. Another explanation to the mixing of asteroids, in specific regions of the MAB, is the constant evolution of the MAB. Upon impact, asteroids release fragments of small sizes (<40 km) that can be affected by Yarkovsky effects (diurnal–nocturnal thermal effects affecting orbitals). The Yarkovsky effect triggers mixing of asteroids that can be ejected when encountering major resonances—thus, depleting the MAB.

1.3.3 Classification of meteorites

The classification of meteorites is based on mineralogical, geochemical and isotopic compositions (oxygen), as well as petrographic characteristics (e.g. chondrules, melting, recrystallisation, igneous textures, abundance of metals). The major subdivisions for the classification are (see Fig. 4 for a simplified meteorite classification based on Rubin 1997 and Weisberg et al. 2006):

– *Chondrites* are primitive meteorites. The principal characteristic of chondrites is the presence of chondrules (spherical grains of silicate composition formed by melting/recrystallization)—not all chondrites have chondrules, this depends on hydrothermal or thermal metamorphism. Distinct isotopic compositions or petrographical and mineralogical characteristics help to classify chondrites in different groups in the *class* > *clan* > *group* scheme (e.g. H, L and LL OCs; CI, CM, CO, … carbonaceous chondrites).
– *Primitive achondrites* originate from parent bodies that did not differentiate until isotopic equilibrium, and thus have similar isotopic, mineralogical or petrographical composition of chondrites with partial melting, complete melting, or complete recrystallization.
– *Achondrites* have isotopic, mineralogical or petrographical composition of differentiated bodies (e.g. iron meteorites as core fragments of differentiated bodies).

In addition to the classification summarized above, there is the petrographic classification (Van Schmus and Wood 1967, Weisberg et al. 2006). This classification focuses on petrographic features (e.g. chondrules, matrix), mineralogical composition, and the degree of aqueous alteration or thermal metamorphism (e.g. ordinary or enstatite chondrites). This classification is important to distinguish chondrites that have lost their pristine structure (e.g. chondrules). There are 6 petrographic types:

– 1–2: aqueous alteration, between 150 and 400ºC (specific to carbonaceous chondrites)
– 3: pristine materials, or non equilibrated chondrites
– 4–6: thermal metamorphism between 400 and 950ºC.

The petrographic types can be correlated with depth ("onion-shell" model) due to thermal depth gradients (radioactive decay, ^{26}Al and ^{60}Fe, Alexander 2005; impact heat source and other heat sources such as crystallization heat). This assumption depends on impact events that can produce rubble-pile asteroids by disruption of the parent bodies (Taylor et al. 1987) and polymict breccias of different petrographic types.

1.3.4 Ordinary chondrites

Ordinary chondrites are classified into three groups: H (High in iron), L (Low in iron), and LL (very Low in iron), with increasing amount of oxidized iron, respectively. This affects both the modal, or normative, composition of metals (e.g. kamacite, taenite) and silicates (olivine, pyroxene) in OCs. Each OC group originates from a different parent body because of dissimilarities in chemical and isotopic composition between H, L, and LL OCs. The major phases in OCs are silicates (olivine, pyroxene, feldspar), metals, and iron sulphides:

– Olivine is an orthorhombic nesosilicate of the chemical form $(Mg,Fe)_2SiO_4$. The forsterite (Mg-olivine) and fayalite (Fe-olivine) solid-solution composes the majority of the bulk composition of OCs (35–52 wt%, McSween et al. 1991; 38–58 vol%, Hutchison 2007). Because the amount of oxidized iron affects the Fe content in olivine, the fayalite/forsterite ratio (or mole% of fayalite) is a good marker for OC classification. The mole% in fayalite is 16–20, 22–25, 26–32 in H, L and LL OCs, respectively (Fredriksson and Keil 1964, Norton 2002).
– Pyroxene is an orthorhombic inosilicate of the chemical form $(Mg,Fe)SiO_3$. The enstatite (Mg-pyroxene) and ferrosilite (Fe-pyroxene) orthopyroxene solid-solution is the second major phase of silicates in OCs (26–21 wt%, McSween et al. 1991; 28–16 vol%, Hutchison 2007). The mole% in ferrosilite is 14–20, 20–30, 32–40 in H, L and LL OCs, respectively (Norton 2002). A small amount

of diopside is found in OCs (4–5 wt%, McSween et al. 1991).

- Feldspar (plagioclase) is a triclinic tectosilicate. The albite ($NaAlSi_3O_8$) and anorthite ($CaAl_2Si_2O_8$) solid-solution is the third major phase of silicates in OCs, but the abundance of plagioclase vary little in OCs (9–9.7 wt% for albite–anorthite, McSween et al. 1991; ~10 vol%, Hutchison 2007). A very small fraction of orthoclase is found in OCs (~0.6 wt%, McSween et al. 1991).
- Metals in OCs, or Fe–Ni alloys, are kamacite, α-(Fe,Ni), and taenite, γ-(Fe,Ni) (Taylor and Heymann 1971). Kamacite is the major metal phase in OCs. As expected from the classification, kamacite abundance varies considerably between H, L and LL OCs (18–4 wt%, McSween et al. 1991; 10–2 vol%, Hutchison 2007).
- Troilite, FeS, an iron sulphide, is one of the principal phases in OCs (5.5–5.9 wt%, McSween et al. 1991; ~5 vol%, Hutchison 2007). The nickel-rich iron sulphide pentlandite can also be found in OCs (e.g. crystallization from a Fe-Ni-S liquid, Fujita et al. 1999).
- Iron sulphides and metals are often found in eutectic mixtures in OCs (Fujita et al., 1999, Tomkins 2009, Mare et al. 2014). The melting point of the mixture corresponds to its chemical composition (Ehlers 1972, Sharma and Chang 1979) and often lower than the individual phases, from 1182 K, LL OCs, to 1237 K, H OCs, depending the Ni content and corresponding to 31.6 wt% of sulfur (Mare et al. 2014). Once an eutectic composition starts to melt, it will either enrich the partial melt with iron (Fe + melt) or iron sulphide (FeS + melt), increasing the melting temperature of the composition accordingly. The abundance of FeNi and FeS grains in contact (or mixtures) is >80% of the total wt% of the grains.

Other phases, such as phosphates (apatite), chrome oxides (chromite, $FeCr_2O_4$), and titanium oxides (ilmenite, $FeTiO_3$), are found in OCs in smaller amounts (<1 wt%, McSween et al. 1991).

Porosity in OCs range from 0% to 20% with mean porosities between 5% and 10% (Consolmagno et al. 2009). There is no correlation with the petrographic type of OCs, but shocked OCs show lower porosities (5–10%) than unshocked OCs (>10%). Less porous OCs are meteorites that have been processed by (multiple) shock compression and by thermal metamorphism, thus precursors of OCs may have showed very high porosities (>50%, Bland et al. 2014).

1.4 Shock waves

To proceed with impact cratering and shock metamorphism, it is important to understand principles of shock physics and shock waves (Zel'dovich and Raizer 2002, Melosh 1989, Davison 2008, Ben-Dor et al. 2000).

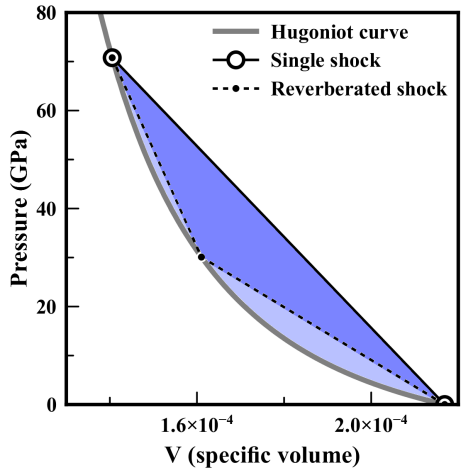

Fig. 5. Hugoniot curve for specific volume and pressure in troilite (this thesis). Because the Hugoniot curve is not a thermodynamic path, the Rayleigh lines (dark lines) illustrate single or multiple shock increases (reverberation). The blue areas between the Rayleigh lines (single or multiple shock) and the Hugoniot curve correspond approximately to the internal energy or the residual energy after release. The actual release adiabat is often approximated by the Hugoniot curve.

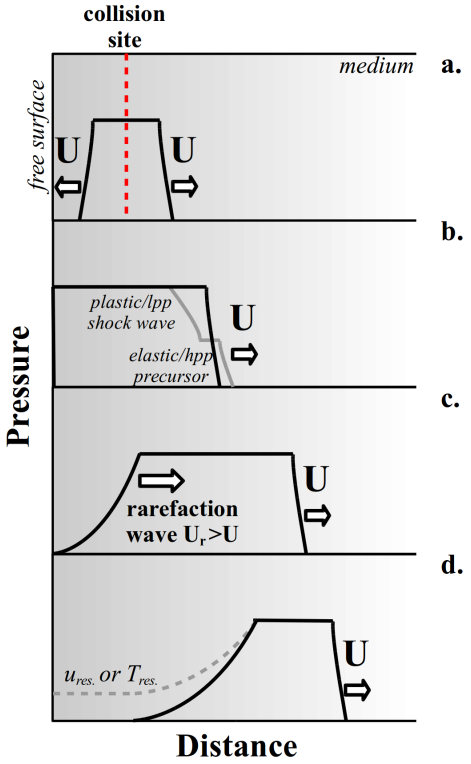

Fig. 6. Schematic representation of the shape of a shock wave initiated by a collision in a medium finite to the left. a–d) progression of the shock wave through time. U – shock wave velocity, U_r—rarefaction wave velocity, $u_{res.}$—residual particle velocity, $T_{res.}$—residual temperature, lpp—low pressure phase, hpp—high pressure phase.

A shock wave is initiated when the wave amplitude of an elastic or plastic wave overcomes the strength of the material and the propagation speed is higher than the speed of sound in gases, liquids, or solids.

When propagating in the medium, the shock wave causes changes in the material thermodynamic state: density (ρ), internal energy (E), pressure (P), temperature (T), particle velocity (u_p), stress (σ). The change in density may be expressed by the specific volume V with $V=1/\rho$. The system, when released from the shock wave, retains some particle velocity (residual velocity) or temperature (release temperature, post-shock temperature). The shock wave conserves mass, momentum and energy.

Knowing the initial conditions of the system three Hugoniot equations can be derived to describe the conservation of mass,

$$1:\ \rho_0 U=\rho\left(U-u_p\right)$$

momentum,

$$2:\ P-P_0=u_p\rho_0 U$$

and energy,

$$3:\ E-E_0=\frac{1}{2}\left(P+P_0\right)\left(V_0-V\right)$$

These equations provide a link between the thermodynamic state of the material in front and behind the shock wave (ρ, or V, P, E, shock wave velocity U, and u_p). Especially with Eq. 3, we can describe a simple shock Riemann problem in the $\delta P/\delta V$ space. It is illustrated in Fig. 5 where the change of pressure and specific volume is outlined for troilite (used in my thesis). The dark lines in Fig. 5 are called Rayleigh lines and show the change of pressure from P_0 to P and V_0 to V in case of single or multiple shocks (e.g. reverberation).

1.4.1 Shock front and decay

Fig. 6 depicts a shock wave propagating across a solid medium. This shock wave originates from a collision between a finite medium (Fig. 6a) with a free surface (void), and a continuous medium, both made of the same material. When two mediums collide at a velocity high enough to generate a shock wave, two shock fronts are initiated, propagating in opposite directions (in 1-D or 2-D planar frames) with a velocity U. The shock acts upon the medium and changes its thermodynamic state as stated previously.

When a shock wave reaches a free surface (Fig. 6b), it experiences a phase change and is reflected, initiating a rarefaction wave propagat-

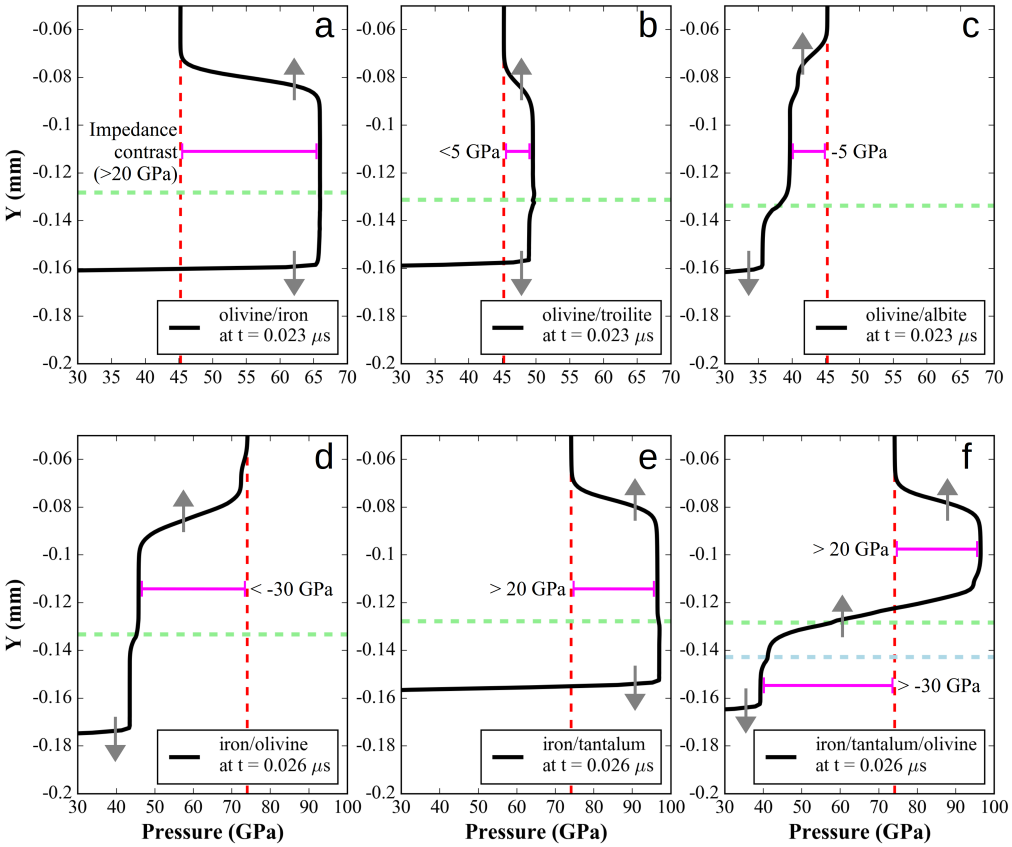

Fig. 7. Pressure profiles of a shock wave propagating from top to bottom, at time *t*, through different material boundaries (horizontal dotted lines). Vertical dotted lines are the nominal pressures in the top material, arrows are directions of propagation. The iSALE model used to produce these profiles is similar to that from Paper I, using layers only. In legends are shown the sequences of materials from top to bottom in the profiles.

ing in the opposite direction (Fig. 6c). This wave releases the material from shock pressure. It is faster than the initial shock wave as depicted in Fig. 6c/d, and overtakes the shock front causing a rapid decay of the shock pressure.

As described above, the shock wave conserves mass, momentum, and energy, but it does not conserve entropy. The entropy increases upon shock compression and, as a consequence, the medium retains some velocity (residual particle velocity, Fig. 6d, $u_{res.}$) and heat (residual temperature, Fig. 6d, $T_{res.}$). A few initial material properties may change after shock compression (e.g. porosity or density). As the shock wave attenuates, it reverts to a strong plastic wave with an elastic precursor, and eventually to an elastic wave before it decays completely.

1.4.2 Impedance contrasts

When an elastic, plastic, or shock wave, encounters a free surface, which possesses no sound speed or pressure and density (e.g. interface between rock and void), the pulse is reflected into the medium as a tensile wave to conserve energy and the particle velocity at the free surface is doubled (summing the particle velocity from both compressive and tensile stresses).

However, if the wave encounters an interface with a medium possessing a lower impedance, the pulse is reflected back as a tensile stress with

lower intensity, and the original pulse propagates beyond the interface with lower intensity as well. In case the interface connects with a medium of higher impedance, the reflected pulse is now a compressive stress of lower magnitude and the continuing pulse is a compressive stress of stronger magnitude. Such reflections at interfaces are very important if a shock wave propagates in heterogeneous mediums composed of zones (grains) of different impedances.

The impedance can be written as (Davison 2008):

$$Z = \rho_0 U \quad (4)$$

where ρ_0 is the density and U the shock wave velocity. Fig. 7 shows the propagations of a shock wave, at fixed time t, through different material boundaries (names in legends). The materials used in Fig. 7 are those used in the thesis; they are, sorted by ρ_0 (i.e. impedance), albite (6% porosity), olivine (6% porosity), troilite, iron, and tantalum. Fig. 7a–c are typical material boundaries found in OCs. Fig. 7d–f are boundaries that can be found in shock-recovery experiments. In general, two directions of shock wave propagation are observed in Fig. 7, but in Fig. 7f, there is at least three directions of propagation from the two boundaries.

1.4.3 Shock wave deformations

In 2-D, or 3-D, shock waves are disturbed by phase changes and irregular interfaces, modifying shape, intensity (see Fig. 7), and direction of propagation. Such disturbance is illustrated in Fig. 8 by particle velocity vectors corresponding to the shock wave direction of propagation. The wave propagating in pure olivine, and reaching an irregular grain boundary of pure iron, will diffract from the top of the iron grain, and in the shock front along the boundary of the grain to the bottom. Upon reaching the bottom of the

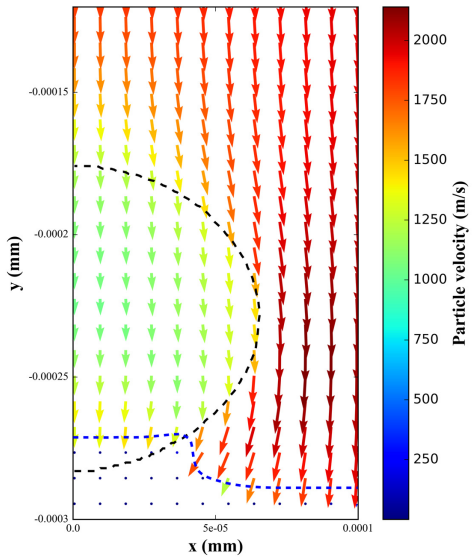

Fig. 8. 2-D Particle velocity vectors in an iSALE model (Paper II) featuring a rounded iron grain (dashed black line) surrounded by olivine. The shock wave propagates from top to bottom and is depicted by the dashed blue line.

grain, the diffracted shock wave will collide and generate a strong rise in pressure (Davison 2008). We also see that the shock front in olivine is ahead of the shock front in iron (higher propagation velocity).

1.4.4 Equations of State and Hugoniot data

Equations 1–3 illustrate well the thermodynamic state of materials in front and behind the shock wave. But for materials such as rocks, minerals, or pure elements, more complex equations can be used to better represent phase and state changes, and improve the accuracy of thermodynamic changes. They are called Equations of State (EoS) and have the basic form:

$$P = f(V,E) \text{ and } T = f(V,E) \quad (5)$$

In my thesis I had to choose EoS for materials I used in my models. The two EoS I chose were: the Tillotson EoS (Tillotson 1962, Brundage 2013) and the more complex Analytical EoS (ANEOS, Thompson and Lauson 1972, Benz et

al. 1989, Melosh 2007). The Tillotson EoS parameters are: a, b, α, β, and B (Pa), material bulk modulus A (Pa), initial and incipient vaporization material densities ρ_0 and ρ_{IV} (g/cm^3), initial, incipient, and complete vaporization material energies E_0, E_{IV}, E_{CV} (J/kg), and finally μ, the strain (η - 1). In the compression phase of the solid and liquid state, the Tillotson EoS take the form:

$$6: \quad P(\rho,E) = \left[a + \frac{b}{E/\left(E_0\eta^2\right)+1}\right]\rho E + A\mu + B\mu^2 \quad \left(\rho \geq \rho_0, E \geq 0\right)$$

Although ANEOS are usually available in shock physics codes for iron, olivine, and other common materials, I had to parametrize Tillotson EoS for troilite, albite, and tantalum and using Hugoniot data (McQueen et al. 1967, Ahrens 1979, Marsh 1980, Mitchell and Nellis 1981, Brown et al. 1984, Ahrens et al. 1998, Trunin 2001, see section 2.2.1 for more details) to determine the best fitting parameters for Eq. 6 in the ρ–P space.

Another important and useful expression is the linear relationship between particle velocity u_p and shock wave velocity U:

$$7: \quad U = C + S u_p$$

with C and S, line parameters. In my thesis, Eq. 7 was used to simplify the estimation of the residual energy (or residual temperature) after release of shock pressure (see Fig. 5; Artemieva and Ivanov 2004, Fritz et al. 2005). The melting temperature of materials rises with pressure and materials remain solid until the shock temperature exceeds the melting temperature at fixed pressure. However, upon release of the shock wave, materials start to melt if the residual temperature is higher than the melting temperature.

1.5 Impact cratering

Because my thesis is related to shock metamorphism, it is important to understand the principles of impact cratering. Indeed, impacts can trigger shock and thermal metamorphism of the impacted body, modifying the body's properties (Davison et al. 2012, Stöffler et al. 2018). Impact cratering (Melosh 1989, Holsapple 1993) is a major process in the solar system, since the origin of planetary accretion, and it shapes the landscapes of planetary bodies. The impact energy is partitioned between the impactor and the target, causing fracturing, heating, melting, vaporization and ejection of material. Impact processes may play a role in the formation of chondrules, however their origin is not yet understood (Lichtenberg et al. 2018).

Traces of impact craters are abundant in the solar system such as on the Moon, Mars, asteroids, Earth and other planetary bodies. If the bodies are not subject to erosion or strong modifications, like on Earth, the size-frequency distribution of craters can be used as a dating tool for planetary surfaces (McEwen and Bierhaus 2006).

1.5.1 Impact cratering stages

Here, I briefly describe the mechanisms of impact cratering. Upon impact of a projectile into a target, the formation of the crater results from three distinct stages (Melosh 1989):

– *The compression stage*: upon impact, the energy delivered by the impactor (simplified as the kinetic energy, $E_{kinetic} = ½ mU^2$) is distributed between two shock waves propagating in both the target and the impactor (see section 1.4.1). The shock wave affects the target/impactor properties such as the density, temperature, or particle velocity, and triggers compression of the material (see section 1.4.4), deforming the target and impactor with first ejection of material. The shock wave propagates radially into the target and the impactor. As it reaches the free surface of the impactor, the shock wave starts to decay.

– *The excavation stage*: once the shock wave decays in the target and projectile (release), the excavation stage takes place. Due to the rest particle velocity in the target upon impact, the material will continue to move radially from the impact zone and excavates to form the transient crater. During this stage, material is ejected outward the crater to form an ejecta blanket surrounding the crater.
– *The modification stage* occurs when the movement of particles is decelerated due to the strength and cohesion of the deeper material at rest or only weakly affected by the decaying shock wave, and by gravity. The material that has been excavated to the crater rim, and steep walls of the transient crater, will fall back to the centre of the crater if gravity overcomes the strength of the excavated structure. This leads to additional intermixing of molten and fragmented materials (breccia) in the crater, such as during the excavation stage.

1.5.2 Collisions between asteroids

Collisions between asteroids are common in asteroid belts. It is one cause for the evolution of the MAB as we know it (Michel et al. 2015). Impact processes on asteroids strongly affect their composition, internal structure, dynamics, and shape. Because of asteroid low gravity, craters on asteroids are mostly strength dominated (depending on the size of asteroids), and they often exhibit the morphology of simple craters (bowl-shaped craters) with diameters proportionally larger than craters on planets and large moons.

Crater formation, shock effects, and melting on asteroids depend on impact velocity, porosity, and the internal structure of the body (Davison et al. 2012):

– *Impact velocities in the MAB* are represented by a non-Gaussian with mean value of 5.3 km/s and probability of impact velocity of 4.4 km/s (Bottke et al. 1994, O'Brien et al. 2011, Vedder 1998). The impact velocity goes up to >10 km/s for most of the statistical analyses.
– *Porosity of asteroids* depends on the composition. S-type asteroids, hosting OCs with densities >3.4 kg/m^3, are characterized by a large range of densities (i.e. porosities) with an average of 2.7 kg/m^3 and porosities ranging from <10% (Vesta, Massalia), to 35% (Ida) and >50% (Britt et al. 2002, Carry 2012) with average porosity of 25–30%.
– *The internal structure of asteroids*, from monolithic to rubble-pile asteroids (reaccretion; Britt et al. 2002), implies both macro- and micro-/porosities. Macroporosity denotes the large cracks and voids from previous impact events and post-impact reaccretion (gravity) on an asteroid, whereas microporosity discerns the internal porosity of boulders, loose material, and the regolith surface. Thus, a rubble-pile asteroid can be composed of cohesive boulders of low porosity held by loose material of higher porosity and void.

Melting on asteroids occurs at lower impact velocities if porosity is higher (Davison et al. 2010), but it can be assumed that melting will not occur in all areas of an impacted asteroid (porosity of rubble pile asteroids is heterogeneous). Also, the more porous an asteroid is, the faster a shock wave attenuates, affecting smaller volumes of material—depending on the impacted area (boulder or loose surface).

Impact processes on asteroids can be disruptive, ejecting fragments of asteroids, and form asteroid families (Michel et al. 2002). In Asphaug et al. (1998), they show that the structure of an asteroid affects the outcome of the impact and whether the asteroid is disrupted by the shock wave or not. For example, they illustrate the buffering effect of a rubble-neck between two boul-

ders of a monolithic asteroid. The rubble-neck prevents the second boulder from being too much affected by an impact on the first boulder, which will be strongly damaged by the shock wave.

1.6 Shock matamorphism

Upon impact, the shock wave induces shock features in rocks and minerals due to high pressures and temperatures with potential melting. The study of shock effects on rocks and minerals is called shock metamorphism. Shock metamorphism has been studied in variety of materials from planetary rocks (e.g. French 1998), to meteorites (OCs, Stöffler et al. 1991, 2018; carbonaceous chondrites, Scott et al. 1992; enstatite chondrites, Rubin et al. 1997; iron meteorites, Rubin et al. 2015), and metals or minerals in shock experiments (Marsh 1980, Trunin 2001). The different degrees of shock metamorphism trace back the impact conditions (e.g. pressures, temperatures, cooling rates).

Progressive shock metamorphism ranges from simple fracturing and deformation at low pressures (e.g. shatter cones, French 1998) of the host rock, and individual mineral phases, to the deformation of the lattice of minerals at higher pressures (mosaicism; planar deformation features, Goltrant et al. 1991, Stöffler et al. 1991). Because of high shock pressures, some minerals undergo a phase transformation (either from the crystallization of a melt or in solid-state), and if they remain stable under ambient conditions they are found in the shocked rocks (e.g. quartz to coesite Goltrant et al. 1991, Gratz et al. 1992; pyroxene to majorite, Stöffler et al. 1991). Diaplectic glass or recrystallization can be observed in plagioclase (maskelynite glass, Stöffler et al. 1991, Rubin 2015). It is not yet fully understood if shock metamorphic features are caused during shock or upon release.

In French (1998), a comparison between regional/contact and shock metamorphism is provided. A transcription of this comparison is given in Table 1.

Based on the variety of shock features that are observed in minerals and rocks, a shock classification has been established. In most cases we divide them into 6 shock stages (chondrites: Stöffler et al. 1991, 2018, Scott et al. 1992, Rubin et al. 1997; terrestrial rocks: French 1998, Stöffler et al. 2018) in addition to whole rock melting. In the case of chondrites, the minerals used for shock diagnosis are olivine, pyroxene and plagioclase—with olivine displaying more charac-

Table 1. Comparison between regional/contact metamorphism and shock metamorphism (French, 1998, modified)

	Regional/contact metamorphism		**Shock metamorphism**
Regional Scale	Affecting large and deep regions of the Earth crust (e.g. plate boundaries, intrusions).		Affecting superficial regions, yet dependent on the impact intensity (projectile size).
Pressures	Lithostatic pressures at depth between 10–50 km, < 1–10 GPa.	<<	10–400 GPa range, highest at the point of impact, quickly decaying radially.
Temperatures	≤ 1000°C, depending on the temperature gradients and initial temperatures of the intrusive bodies.	<	500–10,000°C. Highest at the point of impact. In general no more than 3000°C in nearby rocks. Possible vaporization and melting.
Strain rates	10^{-3}/s to 10^{-6}/s, slow effects of stress for long periods of time.	<<	10^{4}/s to 10^{6}/s, intense effects of stress for short periods of time.
Time scale	~1 Myr, with slow velocity of the interacting bodies.	>>	Quasi-instant. A 10 km/s shock wave passes through 10 cm in < 10^{-5} s. Formation of a 100 km wide crater < 1 hour.
Mineral phases	Equilibration of mineral phases possible after slow reaction times.		Quenching, preservation of metastable minerals and glass phases due to fast reaction times.

teristic deformations. However, in enstatite chondrites it is more important to rely on orthopyroxenes and sulphide minerals (Rubin et al. 1997). As of today, a shock classification in iron meteorites does not exist because this field of research is not well developed (Stöffler et al. 2018).

1.6.1 Shock features

Below, I list a series of features characteristic of progressive shock metamorphism:

- *Shatter cones* are macroscopic, conical, and striated features in any rock type and of any size (French 1998) with conical apex oriented to the centre of the impact crater. The deformation occurs from low to high pressures (up to 30–45 GPa, Stöffler et al. 2018) and is a key feature in identifying impact craters.
- *Fractures and planar fractures* (French 1998) are a strain-based brittle fracturing of a mineral phase following shock loading and elastic–plastic deformation. However, it is difficult to distinguish them from tectonic events and are not diagnostic of impact events. Fractures happen from low to high pressures (e.g. 5–65 GPa in olivine, Stöffler et al. 2018) and follow orientations of mineral cleavages.
- *Mosaicism* is the deformation and disorganization of the crystal lattice exhibiting mosaic patterns in the extinction under cross-polarized microscope. For example, mosaicism occurs between 15 and 65 GPa in olivine (Stöffler et al. 2018).
- *Planar deformation features (PDF)* are structural collapses, or dislocations, of the crystal lattice following the crystal planes (e.g. {101n} plane in quartz, Goltrant et al. 1992). Amorphism and melting along the planes due to shear deformation can happen (amorphous lamellae). This feature is diagnostic of impact events and occurs at high pressures (30–60 GPa in olivine, Stöffler et al. 2018).
- *Diaplectic glass* is an amorphized mineral that can be produced by shock (e.g. quartz at 5 GPa in a porous sandstone, Kowitz et al. 2013; plagioclase between 20–35 GPa in basalt or meteorites, Ostertag 1983, Stöffler et al. 1991, Chen and El Goresy 2000, Rubin 2015). The transformation from plagioclase to maskelynite is still debated and the nature of maskelynite still under investigation (Chen and El Goresy 2000, Jaret et al. 2015). The maskelynite glass either comes from a "quenched dense melt" at high shock pressures (Chen and El Goresy 2000) or is a solid-state transformation to an amorphous plagioclase (Jaret et al. 2015). The pressure required for maskelynite transformation depends on the Ca content of the plagioclase (lower pressure for Ca-rich and higher pressures for Ca-poor plagioclase, Rubin 2015). The most important feature of diaplectic glass is the absence of flow or melt features, so that the phase retains its original crystal shape (French 1998, Chen and El Goresy 2000).

1.6.2 Shock classification of ordinary chondrites

Table 2 gives a transcription of the shock-classification from Stöffler et al. (1991, 2018) and Fritz et al. (2017) in OCs, with a few observations from my thesis (in italic) in the 35–70 GPa pressure range.

When determining the shock stage of a meteorite, observations of phase changes, such as of olivine to ringwoodite (Stöffler et al. 1991, Walton and McCarthy 2017, Fritz et al. 2017) have to be interpreted with care. Ringwoodite is a phase stable at pressures between 16 GPa and 23 GPa and temperatures between 1900°C and 2000°C (Fritz et al. 2017) and is used as a marker for C-S6 (Stöffler et al. 1991), which stage occurs beyond the stability field of ringwoodite. For ringwoodite to be crystallized, its

temperature and pressure have to cross its stability field during the decompression from shock. It is why ringwoodite appears to be stable in the vicinity of melt veins with localized excursion of temperatures and pressures. However, those melt veins can occur at lower shock stages than C-S6. Thus, the marker for ringwoodite formation in shocked meteorites cannot be used as sole indicator for C-S6 (Fritz et al. 2017).

Finally, polymict breccia, which are the mixing of, for example, the asteroid regolith or loose rocks that have recorded different degrees of shock metamorphism through various impact events, can represent a challenge to the shock classification of meteorites (Stöffler et al. 2018). Furthermore, brecciation will create cracks and openings that can be cause of shock features associated with shocked melt veins (e.g. formation of ringwoodite).

1.6.3 Shock-darkening

The shock melting and migration of iron sulphide and metal melt into cracks of silicate grains of ordinary or enstatite chondrites is called shock-darkening or shock-blackening (Heymann 1967, Britt et al. 1989, Britt and Pieters 1989, 1994, Keil et al. 1992, Kohout et al. 2014)—many of the previous studies incorporated whole rock melting or recrystallization into shock-darkening. The melt forms a network of submicron to 1–2 micron veins in the cracks. Because iron sulphides and metals are opaque phases, the distribution of the melt veins darkens the silicates in the visible and near-infrared light (Kohout et al. 2014).

Shock-darkening is mostly observed between C-S3 and C-S6 (Rubin 1992, Bennett and McSween 1996, Rubin et al. 1997, Schmitt 2000, Wang et al. 2011). If associated to lower shock stages, shock-darkening is observed in the vicinity of shocked melt veins (e.g. from cracks formed by brecciation). However, most of the observations are from C-S5 and C-S6, where shock-darkening affects large areas in shocked meteorites. Estimating the progressive shock metamorphism of shock-darkened meteorites is difficult. Observation of silicate deformation features (e.g. mosaicism, planar deformation features) under optical microscope is impossible if the sample appears opaque to the visible light. Often, shock-darkening is associated with localized melting of silicates, which is characteristic of higher shock stages.

The mechanism behind migration of the metal and iron sulphide melt during impact events is discussed in Tomkins et al. (2013). In shock-darkened meteorites, the melt veins are predominantly composed of iron sulphides (Stöffler et al. 1991, Kohout et al. 2014). The reason for iron sulphide abundance in the veins is the "wetting property" of sulphides against silicates (Tomkins et al. 2013), once sulphides are molten. This wetting property is not characteristic for metals, despite being less viscous than iron sulphides. The silicates act as a capillary pressure system for iron sulphide melt, or other melts, to migrate accordingly, with the requirement of a dihedral angle (depending on surface tensions) between silicate crystals small enough (usually $<60–90°$) for a melt to fill the crystal interfaces (von Bargen and Waff 1986, Cmíral et al. 1998, Gaetani and Grove 1999, Hesse 2018) and, thus, activate the wetting properties of iron sulphides. In Fig. 2, it is also evident that the melt veins do not penetrate into plagioclase which does not exhibit cracks. Thus, shock-darkening is likely independent of the amount of plagioclase glass or melt.

The migration of iron sulphides, or metals, into the cracks is also dependent on the amount of available melt. In Tomkins et al. (2013) they discuss the required pressure or stress to displace a certain amount of melt. During shock compression and decompression of meteorites, the pressure gradient may be sufficient to let large

Table 2. Transcription of the shock classification in ordinary chondrites from Stöffler et al. (1991, 2018), Fritz et al. (2017) with details from this thesis.

Shock stage	Destructive shock effects in silicates		Localized P–T effects	Shock pressure (GPa)[1] at transition + melting range of individual phases	Post-shock temperature increase (°C)[1]
	Olivine	*Plagioclase*			
C-S1 unshocked	Sharp extinction and irregular fractures				
				4–5	10–20
C-S2 very weakly shocked	Undulatory extinction and irregular fractures				
				5–10	20–50
C-S3 weakly shocked	Undulatory extinction, planar and irregular fractures	Undulatory extinction	Intermixed melt veins, opaque veins, and dykes of silicates, metals and iron sulphides		
				15–20	100–150
C-S4 moderately shocked	Weak mosaicism and planar fractures	Undulatory extinction (partially isotropic), PDFs	Strong heating or melting by pore and crack crushing in silicates, relative to the shock stage		
				25–35	200–300
C-S5 strongly shocked	Strong mosaicism, planar fractures, and PDFs	Maskelynite quenched glass, no flow texture	Possible formation of LPP/HPP minerals (eg. ringwoodite, wadsleyite, majorite)	*Troilite melting from ~40 GPa (~35 GPa in eutectics)[2]* *Onset of shock-darkening ~40 GPa*	
				45–60	600–900
C-S6 very strongly shocked	Strong mosaicism, PDFs. recrystallization and brown staining	Shock melted with flow texture, vesicles...		*Upper limit for shock darkening ~60 GPa* *Shock-melting of pure troilite at ~60 GPa, 55 GPa in eutectics[3]* *Olivine and iron melting from ~50 GPa[2]*	
				75–90	1500–1750
C-S7 Shock melted				*Shock-melting of pure iron and olivine >100 GPa (~130 GPa in pure iron, ~100 GPa in eutectic iron)[3]*	

[1] Post-shock temperature increase depends on the modal composition of meteorites and the precursor porosity (mostly at higher shock stages). Each phase heats heterogeneously (especially iron sulphides, and plagioclases). Post-shock temperatures are also very dependent on the metal content (related to pressure reflections increasing silicate temperatures). Pressures are estimated from pure olivine (Stöffler et al. 1991).
[2] Real shock pressure in bulk meteorite: considering impedance contrasts and pressure effects between phases during shock compression.
[3] Shock pressure in pure material (crystalline olivine as forsterite)

amounts of molten iron sulphides migrate into the silicate cracks, efficiently. Silicates have same wetting properties and percolate in the rock once molten (Hesse 2018). Melting of silicates may prevent metals and iron sulphides melt from migrating into cracks at higher shock pressures—metals and iron sulphides will remain as isolated molten phases. Thus, when silicates start to melt, shock-darkening may not occur.

1.7 Numerical modelling and shock-recovery experiments

1.7.1 Hydrocodes

I used the shock physics code iSALE in my thesis to simulate shock compression of OCs. iSALE is a shock physics code based on hydrocodes. iSALE was primarily developed to simulate impact cratering. As described in Collins et al. (2013), impact numerical modelling uses principles of continuum mechanics. The differential equations of conservation of mass, momentum, and energy, can also be written as (Collins et al. 2013):

$$8: \quad \frac{Du_i}{Dt} = g_i + \frac{1}{\rho}\frac{\delta \sigma_{ji}}{\delta x_j}$$

with u, velocity, t, time, g, gravity of the system, ρ, density, σ, stress, x, distance, and i, j, coordinates of the system.

To solve the partial differential equations, EoS and strength models (i.e. "deviatoric stress model") are also required. The EoS used in shock

physics codes relate the pressure P with the density ρ and the internal energy E. The strength model, important in impact modelling (Melosh et al. 1992, Ivanov et al. 1997, Collins et al. 2004), describes the resistance of the material against plastic deformation, which is an important part in the response of material to shock wave compression, in particular if low shock pressures are considered.

Originally, hydrocodes proposed simulations of shock waves in fluids or gases, only (Anderson 1987; e.g. SALE code, Amsden et al. 1980). In the last couple of decades, more sophisticated strength models have been developed, enabling the study of shock-wave-induced processes in solid bodies, even if stresses drop below the Hugoniot elastic limit. The development of the shock physics code iSALE is described as follows:

> *"The iSALE-2D code is based on the SALE hydrocode solution algorithm (Amsden et al. 1980). To simulate hypervelocity impact processes in solid materials, SALE was modified to include an elastic–plastic constitutive model, fragmentation models, various equations of state (EoS), and multiple materials (Melosh et al. 1992, Ivanov et al. 1997). More recent improvements include a modified strength model (Collins et al. 2004) and a porosity compaction model (Wünnemann et al. 2006, Collins et al. 2011)."*
>
> *(iSALE manual, Collins et al. 2016)*

1.7.2 Planar shock-recovery experiments and mesoscale modelling

To study progressive shock metamorphism of rocks, planar shock-recovery experiments are used (e.g. Langenhorst and Deutsch 1994, Langenhorst and Hornemann 2005). In such experiments, a metallic flyer plate, accelerated by explosives (Stöffler et al. 2007), impacts a steel case in which a sample pellet is embedded. The experimental set-up is designed to generate a planar shock wave that propagates in the sample. In the following are described two shock-recovery techniques that are often used:

- The *shock impedance* technique uses a sample thick enough (e.g. 1 or 2 cm) to allow the planar shock wave to propagate in the sample without interferences until the shock wave decays. This technique provides an homogeneous shock compression of the sample (Kowitz et al. 2013). However, the experimental set-up is not optimal for higher pressure load due to the impedance contrast existing between the steel case and the (rock) sample.
- The *shock reverberation* technique uses a thin enough sample (e.g. 0.5 mm, Schmitt 2000) to allow the shock wave to reverberate at the steel interface below and above the sample (Stöffler et al. 2007). The amount of reverberations depends on the sample and driver (buffer) plate thicknesses as well as the shock pulse duration given by the flyer plate thickness (see Schmitt 2000 for experimental set-up examples). Contrary to the shock impedance technique, the pressure in the sample is equalised with the pressure in the steel, allowing for higher shock pressures. However, pressures are still limited by the type of explosives used in the experiment. Although the reverberation technique generates higher shock pressures, the rise in entropy is significantly smaller than in case of a single shock. Illustrated in Fig. 5 by the blue areas, the energy accumulated during shock is estimated by the total area between the Rayleigh lines and the Hugoniot curve in the $\delta P/\delta V$ space. If the final shock pressure results from a multiple shock (Rayleigh lines for reverberated shock, Fig. 5), the accumulated energy, or rise in entropy, is thus significantly smaller than for a single shock.

As an alternative to planar shock-recovery experiments, mesoscale modelling has been suc-

cessfully applied (e.g. Crawford et al. 2003, Ivanov 2005, Riedel et al. 2008, Borg and Chhabildas 2011, Güldemeister et al. 2013, Bland et al. 2014, Davison et al. 2016, 2017). Mesoscale modelling is a fast and cost-efficient approach to study shock compression with the following advantages:

- Any desired pressure can be reached by adapting the flyer plate velocity and size.
- Reverberation effects can be avoided by using arbitrary flyer and buffer plates made of the same material as the sample plate.
- Any kind of samples can be used with custom compositions (matrix, inclusions, pores), and strength/thermal properties.
- Shock wave interactions can be observed at any time of the simulation—in shock-recovery experiments, only the final state of the sample is observable.
- Pressures, peak shock pressures, temperatures, and other parameters, can be recorded at any time of the simulation.
- Different geometries, 2-D planar, 2-D cylindrical symmetry, and 3-D simulations, can be used.

Mesoscale modelling can also provide with dynamic insights into shock-recovery experiments if the models are set up accordingly (e.g. Kohout et al. 2012)

1.7.3 Spherical shock-recovery experiments

In spherical shock recovery experiments, a spherical sample is embedded in a spherical steel ring (Wilson 2001, Bezaeva et al. 2010, Kozlov and Sazonova 2012) surrounded by explosives (Wilson 2001). The shock loading of the sample is characterized by: an entry pressure at the outer rim of the sample, a converging rise in pressures toward the centre of the sample (e.g. with pressures >300 GPa at the centre of the sample, Kozlov and Sazonova 2012), and a diverging rise in pressures from the centre of the sample (boiling of the sample can occur in such cases and leave a central cavity, Kozlov and Sazonova 2012).

2 Methods

In this section the shock physics code iSALE and the models used in this research are described in more detail. In addition, a short introduction to the optical and scanning electron microscopes, which were also used in my thesis, is given.

2.1 Hydrocode modelling

A good overview of hydrocode modelling can be found in Collins et al. (2013), upon which the following section is based.

2.1.1 The frames of reference

The computational domain is discretised by a mesh of cells and nodes initialized with material properties. To calculate the flux of material through the computational domain, two types of frames of references are used (Benson 1992, Collins et al. 2013):

- In the *Eulerian frame of reference*, the computational cells are stationary (fixed in space), thus, upon calculation of the material flux, the cells will be partially filled with different materials.
- In the *Lagrangian frame of reference*, cells and nodes are displaced and deformed to retain the mass of the material. Although this frame of reference is useful to observe deformations, it suffers very high deformation rates such as in impact processes (inversion of nodes).

In my research I discretised the computational domain according to the Eulerian frame of reference. Because it was required to trace material boundaries and properties, which is problematic using fixed cells (mixing of materials), I used Lagrangian tracers to keep track of the material position and mass.

2.1.2 Resolution

Accuracy of numerical models depends on the spatial resolution. The right balance between number of cells, or resolution, and computational steps, or time steps, has to be carefully chosen for good computational time and accurate results.

First, time steps are chosen sufficiently small for better accuracy of the computation of material flux through cells. Also, materials can not be transported more than one-fifth of a cell in a time step to avoid loss of information (Collins et al. 2013).

Second, the amount of cells per object must be chosen sufficiently high to allow for accurate numerical results (e.g. distribution of pressures in a given object). In my thesis, similar to impact cratering simulations (cells per projectile radius), I fixed the amount of cells for inclusions in the mesoscale models (cells per grain radius, CPGR). Carrying a series of tests with different CPGR values (Paper I, II, III) allows for a resolution at which numerical results approach an ideal value (i.e. mathematical limit) with the smallest error interval.

2.1.3 iSALE

The iSALE-Dellen manual describes in more detail the code functionalities and how to parametrize models (Collins et al. 2016).

The iSALE code offers several numerical approaches. For mesoscale models, the following units are often used: layers, inclusions, empty space. Material properties, such as EoS, strength and thermal properties, and porosity, are assigned to each unit. The mesh geometry is often 2-dimensional and can be assigned an axis of symmetry on the y-axis for cylindrical simulations of shock wave propagation. Boundary conditions are set up to determine how the material is displaced along the mesh boundaries (e.g. outflow, freeslip). Finally, to generate the shock wave, initial velocity is applied to a specific layer (e.g. flyer plate). More details on the mesoscale numerical set-up are given in Paper I, II, III and reference therein. The numerical set-up is configured through different input files that are best described in the iSALE-Dellen manual.

2.2 The models

In this section I describe each type of model I used in my thesis and the materials assigned to the model units:

- a meso-particle and meso-BMP set-up (Paper I, II, III), Fig. 9a, for studying compression of OCs
- a shock-recovery experimental set-up, Fig. 9b, for studying the dynamics of the reverberation technique
- a spherical shock-recovery experimental set-up, Fig. 9c, for studying the dynamics of spherical shock waves and progressive shock metamorphism in such experiments
- a set-up for asteroid collisions to assess volumes of material shocked at pressures conditions for shock-darkening.

I also applied techniques to compute post-shock temperatures and melting, and used single approaches for eutectic melting. These techniques, and shortcomings for shock compression and shock release (using Tillotson EoS or ANEOS), are explained in detail in my papers—in the supplementary materials for some. These techniques are not implemented in the iSALE shock physics code and I did not quantify associated errors. However, I adopted the calculation of post-shock temperatures and evaluation of peak shock pressures to reduce as much as possible the uncertainties associated with post-shock temperatures, which are not correctly assessed by iSALE (Paper I, supplementary material).

2.2.1 Materials

Here follows a list of the materials I used, or

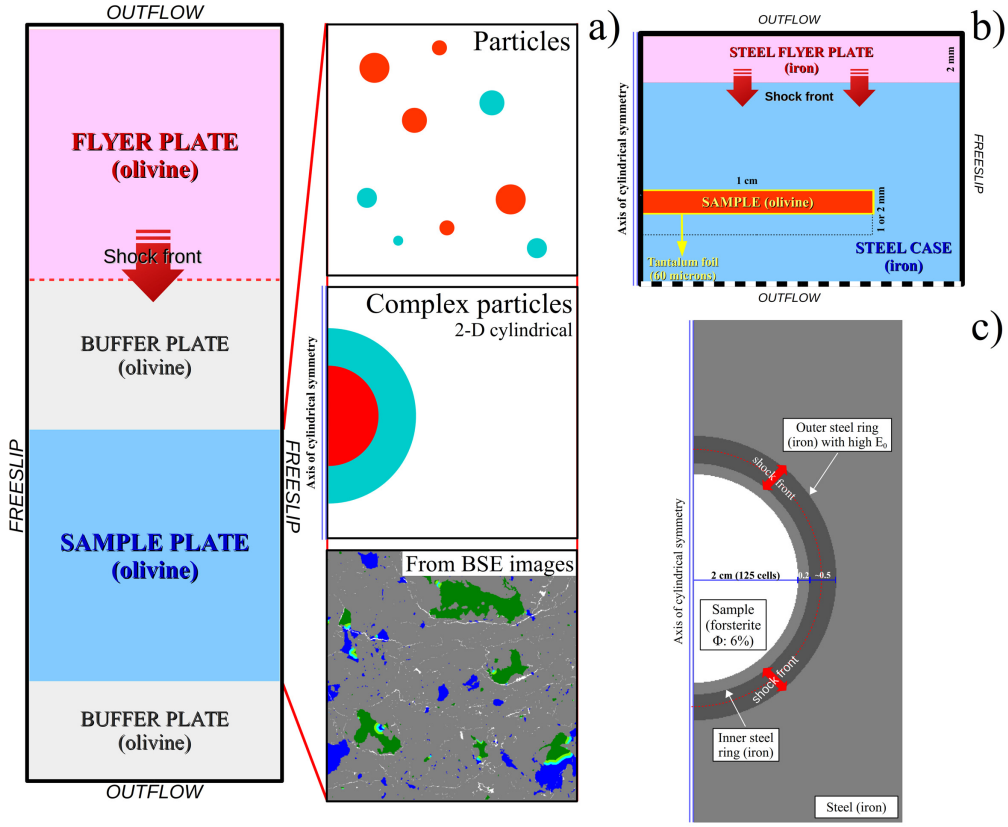

Fig. 9. a) Schematic of a mesoscale model composed of four layers with a sample plate made of different mediums (e.g. particles, complex particles, BMP images; Paper I, II, III), b) schematic of a mesoscale model for shock-recovery experiments using the reverberation technique, c) schematic of a mesoscale model for spherical shock-recovery experiments.

created, to include in my models. Most thermal properties and strength properties of the materials can be found in the published and submitted papers of my thesis. However, tantalum properties and its Tillotson EoS fit are described in more detail in this section. Tillotson EoS fits were used for several materials in my models. The materials are:

- *olivine* using the ANEOS definition provided by iSALE for dunite, which is a forsterite olivine of Fo_{90} composition
- *iron* using the ANEOS definition provided by iSALE for iron to simulate either metals in OCs, or steel, adapting strength properties accordingly—for the shock-recovery models, I used a Johnson-Cook strength model (Vedantam et al. 2006, Kohout et al. 2012) for a DP 590 Steel
- *troilite* with fitted Tillotson EoS to Hugoniot data for pyrrhotite (Paper I and references therein) to simulate the iron sulphides found in OCs—although they don't have same crystal structure (monoclinic for pyrrhotite, hexagonal for troilite), I chose pyrrhotite, from which troilite is the iron-rich variety
- *albite* with fitted Tillotson EoS to Hugoniot data for albitic rock and K–Na-Feldspar (Paper II and references therein) to simulate the albite-rich plagioclase found in OCs
- *tantalum* with fitted Tillotson EoS to Hugoniot data from literature (Marsh 1980, Mitch-

Table 3. Tillotson EoS, thermal, and strength parameters for troilite, albite, and tantalum.

Tillotson EoS parameters	Troilite [a]	Albite [b]	Tantalum
Density ρ (g/cm^3)	4.611*10^3 (4.7*10^3)	2.620*10^3	16.69*10^3
Bulk modulus A (Pa)	0.45*10^{11} (0.8*10^{11})	0.423*10^{11}	1.94*10^{11}
Tillotson parameter B (Pa)	4.0*10^{10}	2.0*10^{10}	1.10*10^{11} (9.4*10^{10})
Internal energy E_0 (J/kg)	14.343*10^6	487*10^6	2.2*10^6
Tillotson parameter a	0.5	0.3	0.5
Tillotson parameter b	1.4	0.6	1.1
Tillotson parameter α	5	5	5
Tillotson parameter β	5	5	5
Incipient vaporization Internal energy E_{IV} (J/kg)	3*10^6	4.72*10^6	2.4*10^6 [(c)]
Complete vaporization Internal energy E_{CV} (J/kg)	5*10^6	18.2*10^6	8.67*10^6 [(c)]
Thermal parameters			
Heat capacity (J/kg/K)	619.23 [(a)] (574 [(b)])	774	126
Melting temperature (K)	1463	1429	3300
Simon's parameter *a (GPa)*	3	1.95	30 [(d)]
Simon's parameter c	4	5.1	2.7 [(d)]
Strength parameters			
Yield strength *Y (Pa)*	2.3*10^9	2.72	0.17*10^9
Poisson's ratio υ	0.25	0.283	0.35

[a] Paper I
[b] Paper II
[c] Iron data
[d] Liu et al. (2008) approximation

ell and Nellis 1981, Trunin 2001, Taioli et al. 2008, Dai and Tan 2009, Rigg et al. 2014). For the tantalum material, Tillotson EoS parameters were already determined in earlier studies (Tillotson 1962, Brundage 2013, Luo et al. 2014). To best fit the EoS to the literature Hugoniot data (see above), I had only to adapt the B fitting parameter (Eq. 6) in the EoS. The A and B fitting parameters mostly act upon the curvature of the Hugoniot curve (e.g. density and pressure Hugoniot curve). Melting temperature, heat capacity and Poisson's ratio of tantalum are 3300 K, 126 J/kg/K and 0.35 (Lide 2003, Wilson 2004), respectively. I used von Mises yield strength criterion for Tantalum with value in between those for tantalum thin sheets (Schmidt and Ogden 1963). Table 3 compiles troilite, albite, and tantalum Tillotson EoS parameters. In Fig. 10 I show the pressure / density and particle / shock wave velocity fields of the Tillotson EoS fitted to the Hugoniot data from literature, for troilite, albite, and tantalum.

2.2.2 Meso-particle and meso-BMP set-ups (Paper I, II, III)

The ideal mesoscale set-up for my research is shown in Fig. 9a, left figure (see section 1.7.2 and set-up used in Güldemeister et al. 2013, Bland et al. 2014, and Davison et al. 2016, for more details on the technique). Specifically for my mesoscale models, I used layers of pure olivine, with same porosity and strength properties. However, heterogeneities (particles or more complex shapes and open pores) were adapted to the research questions. Heterogeneities in my models were (Fig. 9a, see sample plates):

- rounded inclusions of iron and troilite, randomly sized and distributed within the sample plate (Paper I)
- a sample layer set up by a BMP file, repre-

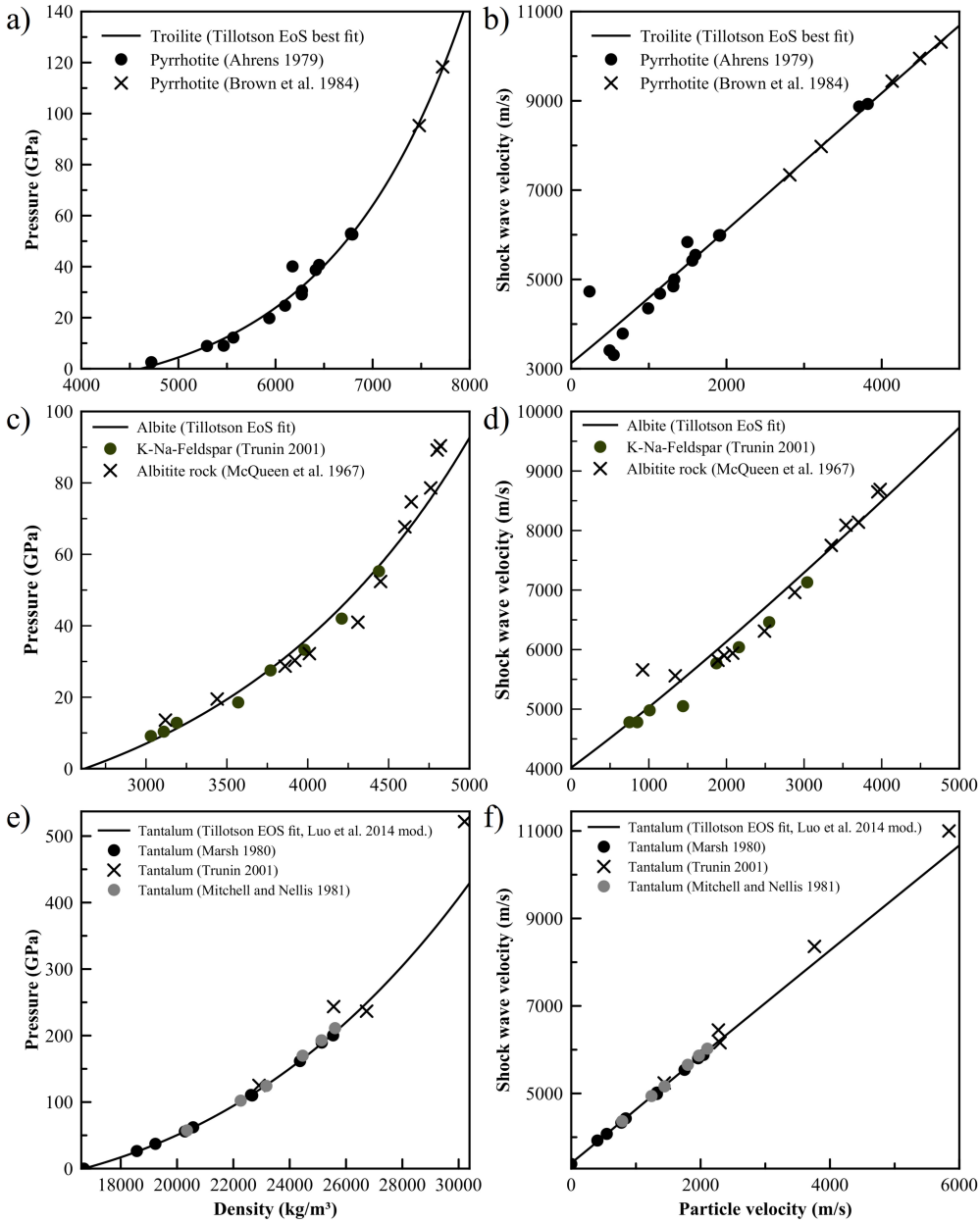

Fig. 10. Literature Hugoniot data and Tillotson EoS Hugoniot fits for trolite (a.b), modified from Paper I, albite (c,d), modified from Paper II, tantalum (e,f) with a,c,e) density and pressure and b,d,f) particle velocity and shock wave velocity fields. No substantial derivation from the data is observed below 200 GPa of shock pressure for tantalum.

senting more complex inclusions with cylindrical symmetry and open pores (Paper II)
– a sample layer set up by a BMP file created from a back-scattered electron (BSE) microscope image with real distribution and shape of phases with open pores and cracks (Paper III).

The use of buffer plates devoid of particles allowed my models to record the pressure (nominal pressure) before the shock wave propagates across the sample plate. This helped me to normalize the results over a range of pressures (e.g. Güldemeister et al. 2013).

All of these mesoscale models are similar, but strength models were progressively improved as well as the complexity of the systematic study. The use of either cylindrical or non-cylindrical symmetry is discussed in Paper II and III.

2.2.3 Reverberation shock-recovery set-up

This numerical set-up reproduced shock-recovery experiments with the reverberation technique (e.g. Langenhorst and Deutsch 1994, Langenhorst and Hornemann 2005, Kohout et al. 2012). Fig. 9b shows the set-up with cylindrical symmetry and additional layers (tantalum foil around the sample). The set-up enables to study: the pressure recorded in the sample after reverberation, the associated shock entropy, the total amount of reverberations, and heterogeneities in peak shock pressures in the sample. Several parameters are recorded from the simulation:

– P_{NSt}, the pressure at the steel and sample interface
– P_N and T_N, the entry pressure and entry peak temperature in the sample—these values are equivalent to single shock pressures
– P_P and T_P, the peak pressure and final temperature in the sample after reverberation.

For studying shock-darkening and efficiency of shock-recovery experiments I didn't need to reproduce individual particles in the sample plate because results from the mesoscale models are normalized to pressures in pure olivine.

2.2.4 Spherical shock-recovery set-up

To simulate spherical shock-recovery experiments on a sphere of olivine (meteorite) with iSALE, I used initial energy rather than velocity to simulate explosives (not available in iSALE) and initiate the shock wave. Initial energy is applied to an outer steel ring, an "explosive" ring surrounding the inner steel ring, as seen in Fig. 9c. Outside the explosive ring, I filled the model with steel, which did not affect the numerical results in sample. The shock pulse propagates inward and outward the explosive ring. Same strength properties were used for olivine (6% porosity, Paper III) and steel (from the shock-recovery set-up described above). One limitation of the technique is the discontinuity at the centre of the sample when the shock wave converges toward it. The converging pressures will be resolved by very few cells, thus the discontinuity will not be correctly resolved, leading to inaccuracy in pressures at the centre.

2.2.5 Asteroid collision set-up

The iSALE models can be set up to study collisions between asteroids (e.g. Housen and Holsapple 2003, Cremonese et al. 2012) by implementing spherical targets or planar targets with spherical projectiles, assuming that pressure and temperature are constant in the interior of the asteroid and the gravity is low. In the following I describe those parameters that are considered to be important in affecting the volume of shock-darkened material in asteroid collisions:

– *Porosity*: to account for the effect of porosity compaction, I used the same porosity model as in my mesoscale models (see details on the ε–α compaction model parameters in Collins et al. 2011). Because I do not consider realistic structures of rubble-pile asteroids,

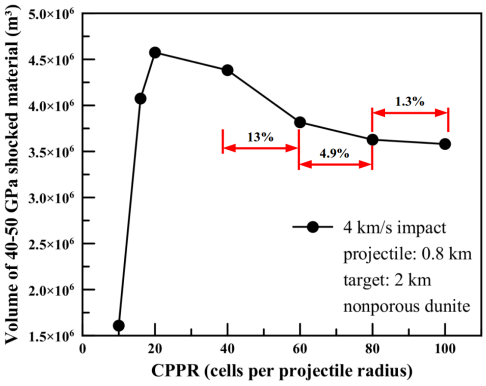

Fig. 11. Resolution in cells per projectile radius (CPPR) used in the asteroid collision model. The results issued from a 0.8 km projectile hitting, at 4 km/s, a 2 km target body. Nonporous dunite material, with strength properties, was used. The recommended resolution is 80 CPPR as the variation from 60 CPPR to 80 CPPR is several percent higher than 80 CPPR to 100 CPPR (see red arrows and corresponding values). Between 10 to 40 CPPR, too small or too high volumes of shocked material are detected. From 40 CPPR, the volume stabilizes with less variation toward 100 CPPR. Extrapolating between 40–100 CPPR values, using 80 CPPR resolution, leads to an error of ~2.7%.

such as in particle codes (e.g. SPH, Deller et al. 2016), I assumed porosity to be homogeneously distributed in the target.

– *Strength properties*: they depend on the internal structure of asteroids. For example, cohesive strength is weaker in rubble-pile asteroids than in monolithic asteroids. Strength is a complex material property that depends on pressure, temperature, strain rate, deformation history (fracturing), and scale (large rock units tend to be weaker than small samples). Therefore the response of rocks to deformation can be only approximated in shock physics codes. For simplicity I did not vary the cohesive strength at different porosities. I used the strength and damage model by Collins et al. (2004) and parameters for this model are listed in Table 4 (taken from Cremonese et al. 2012 who simulated collisions between asteroids).

– *Resolution*: in impact simulations, resolution is measured by the amount of cells per projectile radius (CPPR, e.g. Cremonese et al. 2012). Previous studies have shown that the volume of shocked material determined in models asymptotically increases with resolution (Pierazzo et al., 1997, Wünnemann et al. 2008). In order to determine the resolution required for this study I carried out a series of tests using a dunite 0.8 km projectile impacting a dunite 2 km target at 4 km/s, both nonporous with strength properties as described above. I varied CPPR values between 10 and 100 and determined the volume of shocked material (here, 40–50 GPa). Results are compiled in Fig. 11. To asses the error for different CPPR, I extrapolated the data to "infinite" resolution, which may be considered as the "real" value (Wünnemann et al. 2008). According to this estimation, the chosen CPPR resolution of 80 cells results in an error of 2.7%.

– *Target size dependency*: in addition I carried out a series of models to test whether the size of projectile and target with a fixed ratio of radii ($R_{proj.}/R_{target}$) influences the volume of shocked material between 40–50 GPa normalized to the projectile volume ($V_{Shocked}/V_{Proj.}$). The results of these tests are:
  – Regardless of the size of the projectile and target at fixed $R_{Proj.}/R_{Target}$, the volume of shocked material remained proportionally the same. As shock volume

Table 4. Strength properties of dunite (impact models).

Parameters in iSALE [a]	
Strength (intact) Y_{i0}	50 MPa
Strength (damaged) Y_{id}	0.05 MPa
Limited strength (intact) Y_{ilim}	3500 MPa
Limited strength (damaged) Y_{idam}	3000 MPa
Coefficient of internal friction (intact) μ_i	1.2
Coefficient of internal friction (damaged) μ_d	0.6

[a] from Cremonese et al. (2012)

only depends on $R_{Proj.}/R_{Target}$, it is sufficient to vary the ratio.

– The volume of shocked material increased with decreasing $R_{Proj.}/R_{Target}$ and this is an effect of target curvature (radial shock wave).

However, using the continuum physics of iSALE, it is impossible to study fragmentation of the impacted body and gravity interactions within a fragmented asteroid, and rubble-pile asteroid configurations are limited, in contrast to particle codes (Monaghan 1988, Asphaug et al. 1998).

2.3 Microscope

Observations on a shock-recovered meteorite were carried out with a transmitted and reflected light microscope and with a scanning electron microscope using BSE microscope images. No immersion oil was used for the optical microscope and maximum magnification was 50x; parallel, cross-polarized and retarded cross-polarized lights were used to identify shock features.

3 Research output

In this section I summarize the essential findings in the framework of my thesis that have been published or are submitted for publication. In addition to these findings I provide the section with simulations for reverberation shock-recovery experiments and spherical shock-recovery experiments. I supply observations on microscope of the experimentally shocked Chelyabinsk LL5 chondrite. Finally, I present preliminary results for large scale impact modelling to investigate shock-darkening in collisions between asteroids.

Fig. 12 shows how the different results (published and unpublished) feed into one another and summarizes them with take-home messages. Only one experiment has been carried out during the thesis, which is not sufficient to study shock-darkening in detail. However, a few experimental studies where shock-darkening was reproduced will be presented (Schmitt 2000, Kohout et al. 2018, Petrova et al. 2018).

3.1 Temperature and pressure conditions for shock-darkening (Paper I)

The first topic of my research was to evaluate the exact pressure at which we can observe melting of iron sulphides—major constituent in the shock-darkening agent. I used the model set-up shown in Fig. 9a with rounded metal and iron sulphide particles to mimic OCs. I used nominal pressures, or pressures in pure olivine (Stöffler et al. 1991), as a proxy for progressive shock metamorphism because olivine (as forsterite) shock compression compares very well to shock compression of OCs in term of thermodynamic changes (Schmitt 1995). The modelling concept used in this research is not unique (see references in section 1.7.2), but is the first research focusing on numerical modelling of shock compression of heterogeneous mediums using metal and iron sulphide particles, and olivine matrix.

The results and take-home messages of the systematic study were:

I. At a pressure range of 40–50 GPa the melting of iron sulphide over olivine and metal dominates.
II. Shock wave interactions, such as reflections between metal and iron sulphide particles in the olivine matrix, are a key process for heating and melting phases (impedance contrasts). I investigated on how many reflections can affect a mineral phase (e.g. in few zones, more than 10 reflections from metal and iron sulphide grains to olivine, causing a significant increase of pressures in olivine).
III. Shock heating of olivine is dependent on the abundance of metal particles from LL to H chondrites.
IV. The orientation of elongated grains affects

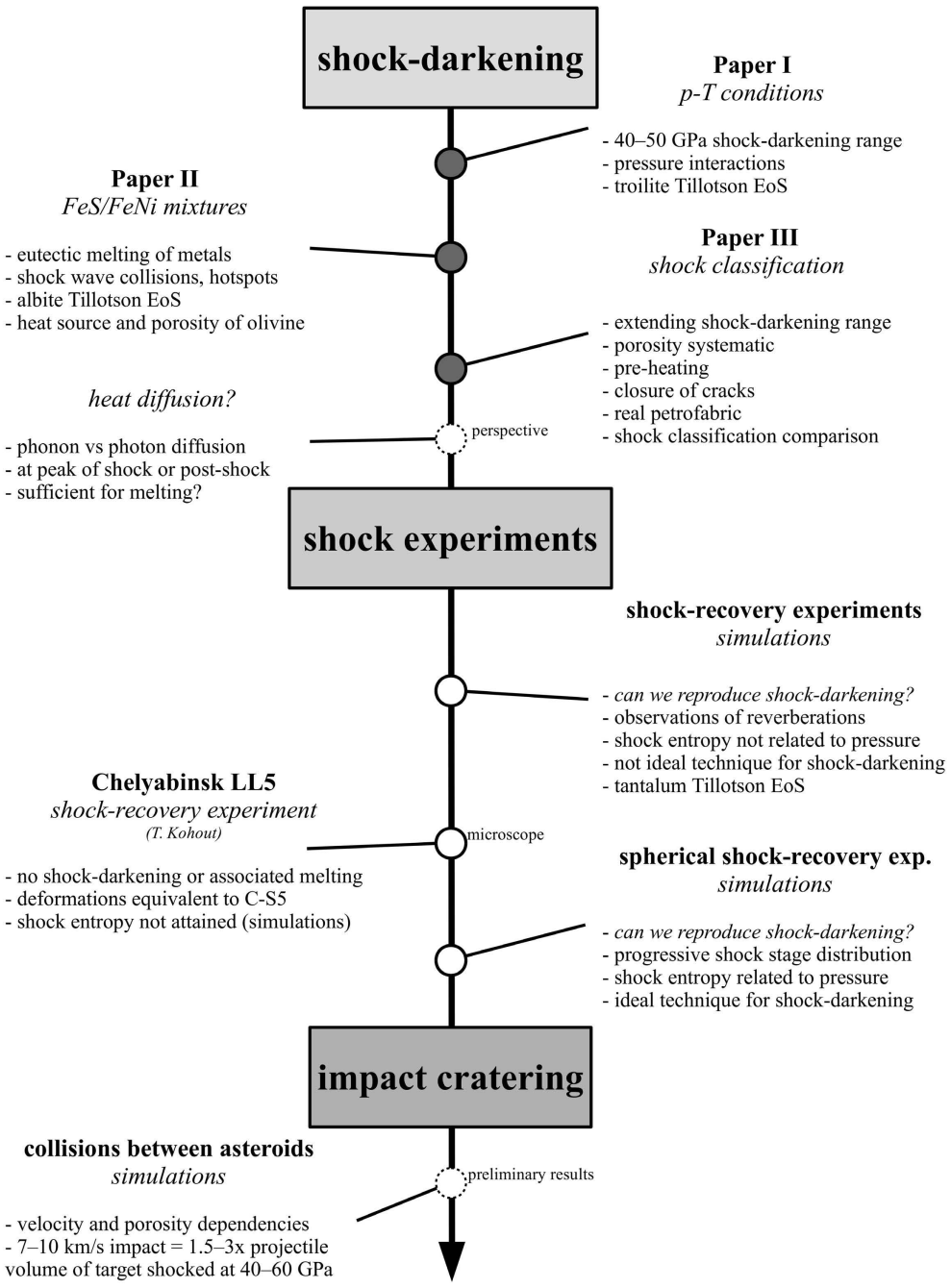

Fig. 12. Flow chart of the thesis research and research output with emphasis on results, aims of the research, or take-home messages, for each topic. Plain circles represent the major output of the research with published or submitted work. Empty circles represent other output of the research that may be part of future collaborations as co-author or first-author. Empty dashed circles are researches in early stage.

shock pressures. Grains oriented longitudinally to the shock wave experience higher peak shock pressures than grains oriented transversally.

V. Comparison between Hugoniot data for enstatite and forsterite showed that the ANEOS for dunite in iSALE is sufficient to simulate either enstatite or forsterite in mesoscale models (see Paper III).

Shortcomings of this research output and new topics of research were:

A) The estimation of post-shock temperatures was accurate for iron sulphide, but not for metal and olivine (no integration of heat capacity over temperature and no heat of fusion). Thus, it was difficult to directly compare the results, and temperature estimates in olivine, with the shock classification of OCs. Also, melting of phases was only estimated by the amount of material at melting point.

B) All iron sulphide and metal particles were isolated and rounded, and no direct interaction between metals and iron sulphides occurred. Metals and iron sulphides are often found in eutectic mixtures in meteorites. Melting of iron, which can be found in the shock-darkening veins, was seldom observed.

C) No realistic representation of grain shapes and distribution in OCs in the sample plate, as all particles were rounded.

D) Porosity was only studied as a material parameter and no pores were resolved in the multiphase models. Also the chosen porosity for olivine was low (6%) and no tests with more porous olivine were carried out.

E) No more detailed illustrations on shock wave propagation in the individual grains were provided.

F) No heat diffusion in the models or iSALE.

3.2 Mixtures of iron sulphides and metals (Paper II)

This part of my research focused on shock wave reflections between metal and iron sulphide particles, and the olivine matrix, to address shortcomings B, D, and E, of Paper I. I investigated different configurations of iron sulphide and metal mixtures in 20 models (examples shown in Fig. 8 and 9a). I assumed simplified eutectic properties between metals and iron sulphides (corresponding to 31.6 wt% of S, see 1.3.4). The shock pressure in the models was 45 GPa. I determined in which scenarios metals start to melt at the given pressure. The discussion briefly focused on how heat diffusion and frictional heating may affect melting. In addition, the effects of pore crushing on an iron layer are investigated. To study the shock entropy of plagioclase, I created a new Tillotson EoS for albite. To investigate how shock compression affects pristine uncompressed OCs, a highly porous olivine matrix was also used. I finally improved estimation of post-shock heating and melting of phases (melt fraction). To summarize:

I. Metals can be found in the shock-darkening network of veins, but under strict conditions of shock wave interactions in eutectic mixtures. However, pure metal remains resistant to shock melting at 45 GPa.

II. Heat diffusion may be considered important to cause melting of metals in zones were the contrasts of temperatures between olivine, plagioclase, or iron sulphide, are high. Contrasts of temperatures between olivine and metal increase if olivine material is more porous.

III. Shock heating of albite is more effective than shock heating of olivine. Peak shock pressures in albite often equalize with the surrounding material peak shock pressures (pressure reflections and impedance con-

trasts between olivine, iron, or troilite; e.g., in Fig. 7c, if an olivine layer is added beneath albite, the pressure in albite will equalise to that of olivine from the pressure reflection at the new boundary).

IV. Insight is given on the shock wave propagation to explain several hotspots that occur, for example, behind grains or at irregular phase boundaries. The models showed that hotspots can result from the superposition of shock waves.

3.3 Shock metamorphism and realistic grain distribution modelling from BSE images (Paper III)

The third part of my thesis dealt with the investigation of shock compression in ordinary and enstatite chondrites with a particular focus on C-S5 and C-S6 (Stöffler et al. 1991, 2018) and points A, C and D of section 3.1. For the model set-up I used BMP images converted from BSE images of meteorites, such as shown in Fig. 9a. This set-up enables combination of open pores, metals, and iron sulphides of realistic shapes in the olivine matrix. In addition, models for enstatite chondrites with pyroxene as the matrix mineral were taken into account. The outcomes of this research topic were:

I. New range of pressures for shock-darkening, from 40 to 60 GPa with the upper limit depending on the porosity of silicates (if highly porous silicates start to melt at lower pressures, it will inhibit shock-darkening), and good comparison with literature data on shock-darkened OCs.

II. I successfully compared the modelling results with the progressive stages of shock metamorphism:
   i. observation of plagioclase partial melting at C-S5 and complete melting at C-S6
   ii. partial to complete melting of iron sulphides at C-S6
   iii. melting of silicates and metals starting at high pressures at C-S6
   iv. localized melting due to crack closure at C-S5 and below
   v. good comparison of post-shock temperatures with the shock classification.

III. Melting features in iron sulphide, metal, and plagioclase, were comparable to literature.

IV. C-S5 and C-S6 can be attained at lower pressures if porosity is higher or the sample is subject to thermal metamorphism before the impact event.

V. Orientation of cracks to the shock wave in olivine affects post-shock heating and melting of olivine—effective shock heating with cracks oriented between 45 and 60 degrees.

This research output concluded the mesoscale modelling of shock compression in OCs. The 40–60 GPa shock-darkening pressure range was now taken as a boundary condition to study shock-darkening in shock-recovery experiments. Moreover, because my results are adjusted to the pressures in pure olivine (Stöffler et al. 1991), modelling of shock-recovery experiments and asteroid collisions can be simulated in mediums made of olivine only.

3.4 Reverberation shock-recovery experiment simulations

A shock-recovery experiment (reverberation technique) on an OC was prepared by my supervisor, Tomas Kohout, and carried out at the Ernst Mach Institute in collaboration with Andreas Holzwarth and Hagen Aurich. The chosen sample was a light lithology Chelyabinsk LL5 chondrite with 6% porosity and shocked by a 55.5 GPa pressure at the interface between steel and sample (P_{NSt}), with a 5 mm steel buffer between the sample and the surface of contact with the 2 mm flyer plate. The 1.7 mm thick and 2 cm wide disc sample was wrapped in a 60 microns thin tantalum foil. Petrographic and

Table 5. Numerical results of the shock-recovery simulations (reverberation technique)

Flyer plate (m/s)	P_{NSt} (GPA)	P_N (GPa)	*std.*	P_P (GPa)	*std.*	T_N (K)	*std.*	T_P (K)	*std.*	P_{rise} (%)	*std.*
2 mm sample, 6% porous, w/ Ta											
1800	37.0	21.8	*0.9*	31.3	*3.2*	529.0	*37.7*	574.3	*53.1*	43.5	*16.9*
2000	42.7	25.3	*1.0*	36.2	*3.7*	576.3	*36.2*	627.6	*54.0*	43.7	*7.6*
2200	48.5	28.7	*1.3*	41.5	*4.1*	621.2	*38.5*	682.2	*58.7*	44.8	*17.6*
2430	55.5	32.9	*1.3*	47.6	*4.7*	679.8	*40.8*	749.0	*65.5*	44.8	*16.2*
2600	60.9	35.9	*1.1*	51.8	*5.1*	725.5	*40.4*	797.7	*66.9*	44.5	*15.9*
1.5 mm sample, 6% porous, w/ Ta											
1800	37.0	21.8	*1.0*	34.0	*1.8*	520.6	*39.3*	577.3	*50.1*	56.8	*13.2*
2000	42.7	25.1	*1.0*	39.5	*1.9*	568.6	*35.6*	632.7	*48.3*	57.3	*10.9*
2200	48.5	28.6	*0.9*	45.2	*1.9*	613.1	*36.4*	688.1	*50.6*	58.3	*8.8*
2430	55.5	32.7	*1.2*	51.9	*2.2*	670.3	*38.1*	756.3	*54.6*	59.0	*10.6*
2600	60.9	36.1	*1.6*	57.7	*2.6*	723.4	*51.2*	824.6	*74.4*	60.3	*10.1*
1.5 mm sample, 6% porous, w/o Ta											
1800	37.0	21.9	*1.0*	31.6	*1.1*	522.5	*41.2*	565.5	*44.3*	44.8	*7.9*
2000	42.6	25.3	*1.0*	36.7	*1.3*	575.4	*32.2*	624.0	*36.7*	45.2	*6.2*
2200	48.5	28.7	*1.0*	42.3	*1.4*	623.6	*28.4*	682.0	*33.8*	47.4	*5.5*
2430	55.5	32.8	*1.1*	48.4	*1.7*	685.1	*24.4*	751.4	*31.0*	47.6	*6.2*
2600	60.9	35.7	*1.8*	53.3	*1.8*	733.0	*24.2*	805.2	*26.4*	50.0	*12.1*
1.5 mm sample, 12% porous, w/o Ta											
1800	37.0	19.0	*1.0*	31.4	*1.5*	660.8	*48.9*	725.1	*51.5*	65.5	*8.2*
2000	42.6	22.2	*1.2*	36.5	*1.7*	736.3	*36.2*	810.4	*43.0*	64.1	*7.5*
2200	48.5	25.5	*1.4*	41.5	*2.1*	808.9	*31.9*	893.2	*40.7*	63.0	*7.7*
2430	55.5	29.5	*1.6*	47.7	*2.4*	897.9	*29.5*	996.1	*39.4*	62.1	*7.4*
2600	60.9	32.3	*1.3*	52.7	*2.5*	967.8	*26.5*	1072.7	*36.1*	63.1	*7.2*
Schmitt (2000)											
2430	55.5	30.9	1.0	54.7	1.3	768.9	39.8	875.6	39.9	77.5	*8.0*
2600	60.9	33.6	1.0	60.1	1.5	840.0	23.9	956.6	29.3	79.3	*8.3*
2840	68.7	37.7	3.1	67.5	1.1	918.4	40.8	1063.9	33.2	80.9	*23.0*
3100	77.7	42.7	3.0	76.4	2.5	1029.8	36.7	1234.8	33.6	80.1	*19.1*

microscope analysis of the experiment showed no shock-darkening or very rare melting of troilite in the shocked sample (see section 3.4.3 for more results).

3.4.1 Estimation of the shock entropy

To know the real pressure load in the sample and the related shock entropy, I modelled the experiment using the shock-recovery set-up shown in Fig. 9b. With fixed cell size of 15 µm, I used a 2 and 1.5 mm thick samples with a 0.06 mm thick tantalum foil, 2 mm flyer plate and 5 mm buffer plate, each resolved with 134, 100, 4, 134, and 333 cells in height. I shocked the samples at different pressures (P_{NSt}), including the experimental pressure of 55.5 GPa, in order to correlate the

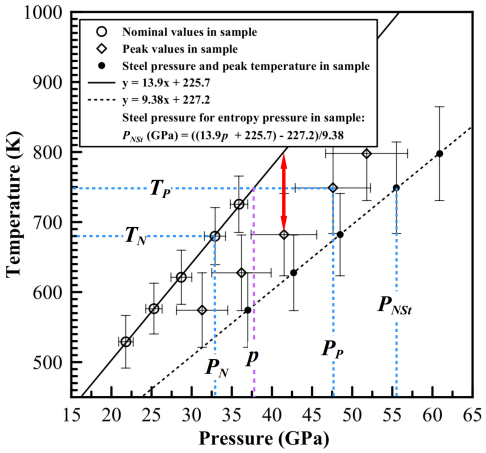

Fig. 13. Numerical results of a shock-recovery experiment using a 2 mm thick sample, 5 mm buffer, 2 mm flyer plate, and tantalum foil, at different pressures in steel. Nominal and peak values in sample are indicated by the fine-dashed blue lines for a 55.5 GPa in steel simulation. The red arrow illustrates the reverberation effect on the shock entropy (decrease) as seen in shock-recovery experiments. The purple dashed line is the shock entropy equivalent pressure p, whereas P_P is the peak pressure related to mechanical deformation in sample. Fitted lines are used to determine an equation to relate P_{NSt} (pressure in steel) and p.

reverberated pressures and shock-heating in the sample. This approach allowed me to estimate whether the pressure–temperature conditions for shock-darkening are attained in the shock experiment at 55.5 GPa of steel pressure. All results presented in this section are compiled in Table 5.

In Fig. 13 I compile the numerical results for the 2 mm thick sample, with P_N and T_N, P_P and T_P, at different P_{NSt} values. Fine dashed vertical/horizontal lines in Fig. 13 illustrate the 55.5 GPa (P_{NSt}) numerical results with values for P_N, T_N, P_P, and T_P of 33 GPa, 680 K, 48 GPa, 750 K, respectively. The fitted line for the peak values in the sample does not superimpose with the fitted line for nominal values in the sample and is shifted toward higher pressures with lower slope. This illustrates well that, at the same pressure, peak temperatures from reverberated shock pressures do not reach the same temperatures as in a single shock pulse (illustrated by red double-arrow in Fig. 13; see also section 1.7.2).

Although an equalization between sample and iron case is partially achieved as a consequence of reverberation of shock waves, melting and heating cannot be correlated to P_P due to the lower shock entropy compared to a single shock (see value p in Fig. 13). In this case, if we want to know the pressure in steel to attain a specific shock entropy equivalent pressure p for shock-darkening in the sample, thus ignoring mechanical effects, one can simply correlate P_N/T_N to P_{NSt}/T_P values. This is illustrated by the equations shown in Fig. 13. In Fig. 14 are shown the results (purple line) for the equation shown in Fig. 13, which enable to estimate the required pressure in steel to obtain the desired shock entropy in the sample, depending on what can be done in reality (e.g. type of explosives). I added results for the 1.5 mm thick sample in Fig. 14, and two other sets of results to show the effects

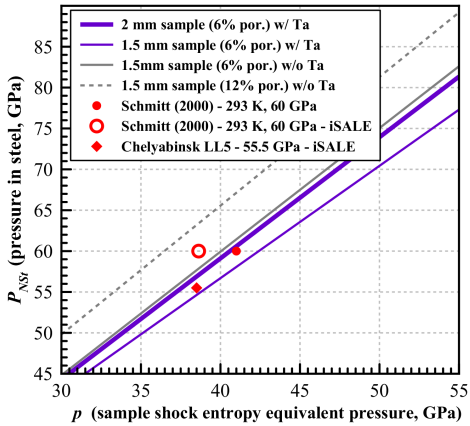

Fig. 14. Required pressure in steel P_{NSt} to obtain a shock entropy equivalent pressure p in sample (using the reverberation technique) after several model configurations. The purple lines are models discussed in this thesis. Grey lines illustrate the effects of tantalum foil and porosity on the final results. The red circles are shock entropy equivalent pressures estimated in Kernouvé H5-chondrite (Schmitt 2000) for a 60 GPa shocked sample where shock-darkening occurred in few zones (hollow marker: iSALE result). Red diamond is the iSALE result for the Chelyabinsk LL5 chondrite shocked at 55.5 GPa of pressure in steel.

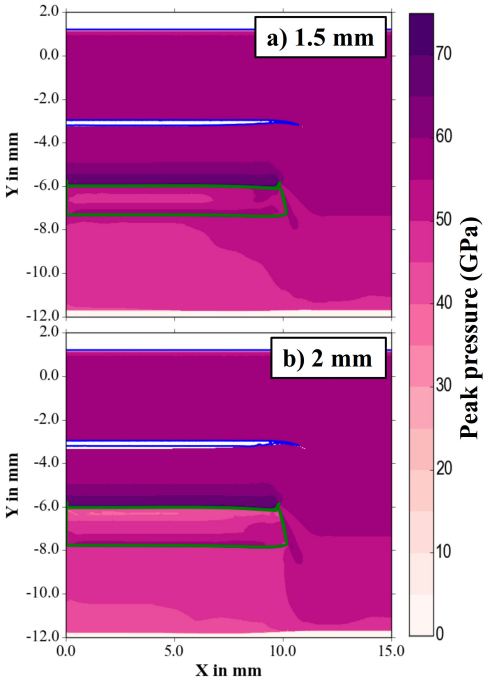

Fig. 15. Peak shock pressures recorded in the shock-recovery experiment simulations with a) 1.5 mm thick sample, b) 2 mm thick sample, with 5 mm buffers, 2 mm flyer plates, and tantalum foil.

of sample thickness, porosity, and presence of tantalum foil. Making such correlations is important for studying shock-darkening in OCs using the reverberation technique in shock-recovery experiments. Thus, in the real experiment, and because shock-darkening is very dependent on post-shock heating, the shock entropy was not sufficient for shock-darkening with a value of ~50 GPa of peak shock pressure and ~38 GPa of shock entropy equivalent pressure in sample (see red diamond in Fig. 14).

3.4.2 Heterogeneities and effect of tantalum foil

In the 2 and 1.5 mm thick sample models I also observe that peak shock pressures are not homogeneous, as seen in Fig. 15a/b. Heterogeneities are explained by an early decay of the shock wave pulse preventing complete reverberation of pressures in the sample and equalization with the pressure in steel. More specifically in Fig. 15b, the reflection occurring at the interface between steel/tantalum at the bottom of the sample was decayed by the rarefaction wave before it could reach the top of the sample. In Fig. 15a, a second reflection occurred at the top of the sample before it was also decayed by the rarefaction wave. From models shown in Fig. 15, the peak shock pressures in the samples never equalised with the pressure in steel. To prevent an early decay of the shock wave, the best set-up for the reverberation technique requires thinner samples or buffers, and thicker flyer plates, if possible (e.g. 0.5 mm thick sample used in Schmitt 2000 for a 60 GPa pressure in steel).

For more details, in Fig. 16 are shown pressure profiles of the shock wave propagating through the models with 1.5 mm thick samples (6% porosity), with and without tantalum foil, at different time steps. Fig. 16 illustrates well the effect of tantalum foil in rising the sample pressures (P_N and P_P) due to impedance contrasts, although the shape of the shock wave is similar in both models. The delay of the shock wave in the model without tantalum foil, indicated by the purple box in Fig. 16, is explained by a slower propagation of the shock wave (lower pressure rise). The rarefaction wave is also indicated in Fig. 16. The models used in this figure are simplified models from the model geometry shown in Fig. 9b (10 cells width, and no sample corner), but with a resolution ~5 times higher in y-axis.

3.4.3 Microscope observations

As detailed above, the experimentally shocked Chelyabinsk LL5 chondrite, at 55.5 GPa of pressure in steel, did not display shock-darkening because of insufficient rise of entropy. However, mechanical deformations characteristic of C-S5 (Stöffler et al. 1991, 2018) are observed at the equalised peak shock pressure of ~50 GPa:

– PDFs (not abundant; see Fig. 17 for an ex-

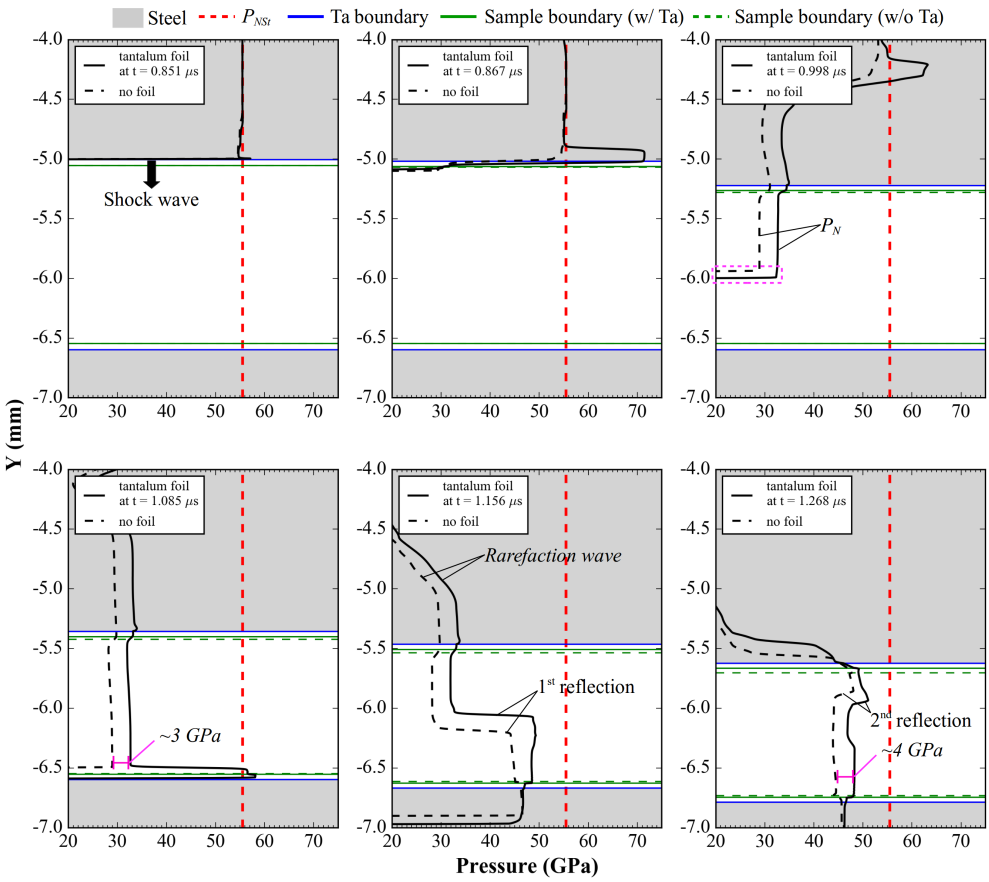

Fig. 16. Influence of tantalum foil on pressures, with profiles at time *t* (time since impact) of a shock wave in reverberation shock-recovery experiments. The models are for 6% porous and 1.5 mm thick samples, with and without tantalum foil. The purple box shows the delay of the shock wave propagation due to a contrast of pressure and shock wave velocity between the two models. The two models only used layers of 10 cells in width, with a vertical resolution ~5 times higher than the models presented in the shock-recovery experiment simulations. The steel material extends to the sample (green dotted lines) for the model without tantalum foil.

ample of PDF features in olivine)

– strong mosaicism (abundant).

Maskelynite was rarely observed under optical microscope—shock entropy was not sufficient for significant formation of maskelynite.

Using BSE images of the sample, seldom melting of troilite was observed. Only did troilite melt in the vicinity of plagioclase or at bottom of grains in few cases (relative to the first shock wave pulse direction in the experiment). In Fig. 18 I compile such observations with Fig. 18a, a cluster of unmolten troilite grains, Fig. 18b/c, intermixed melting of troilite and plagioclase and melting at bottom of the grains. Eutectic mixture between kamacite and troilite is observable in Fig. 18c. Such melting features were discussed in Paper II and III to explain intermixed melting of troilite and plagioclase and melting at bottom of grains. However, these features may not necessarily originate from the shock experiment as the unshocked sample is of C-S4, below 35 GPa. In Paper III, albite starts to melt locally below 35 GPa, and because it has a melting temperature similar to troilite, intermixing of troilite/plagioclase melt is thus possible at the limit of C-S4 and C-S5.

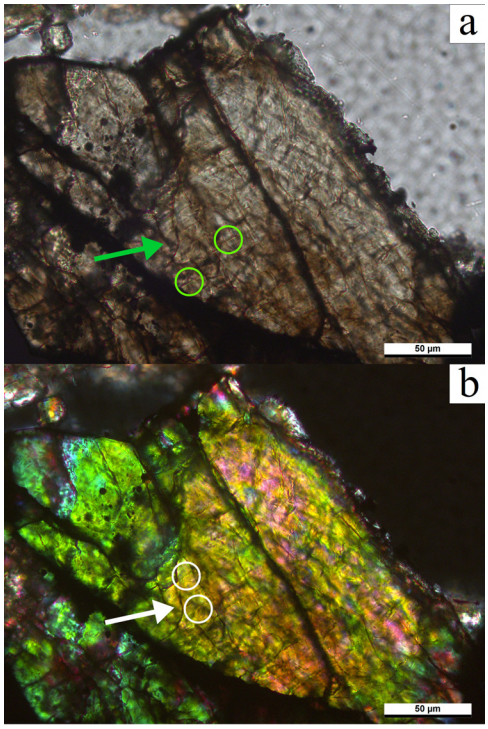

Fig. 17. Planar deformation features in olivine in the experimentally shocked Chelyabinsk LL5 chondrite. a) planar polarized light and b) cross-polarized retarded light. Arrows indicate the most affected grain and circles emphasize a few planar deformation features.

3.5 Spherical shock-recovery experiment simulations

To compare the reverberation shock-recovery experiments with the spherical shock-recovery experiments, I used the model set-up shown in Fig. 9c. I adapted the model to obtain, roughly, similar results from a spherical shock experiment on a 4 cm Chelyabinsk LL5 chondrite sphere, detailed in Kohout et al. (2018) and Petrova et al. (2018). The explosive source in the experiment is approximated with a 4 MJ/kg specific energy loaded in the explosive ring and the resolution of the sample is 126 cells in radius.

To analyse the results, I recorded the pressures, peak shock pressures, related shock stages, and particle velocities in the model. Snapshots in Fig. 19a/b, are taken at model time of 3.22 and 3.68 µs and they display the following:

- The direction and relative magnitude of particle velocity vectors in 2-D are shown in Fig. 19a/b.1, and the x-axis particle velocity components from a horizontal cross-section of the model at the largest section of the sample are shown in Fig. 19a/b.3. Negative velocities in the cross-section graphic represent a direction of propagation inward, or to the left, of the model, and vice versa.
- The propagation and intensity of the shock wave are displayed by 1) peak shock pressures from a horizontal cross-section of the model at the largest section of the sample in Fig. 19a/b.2, and by 2) instant pressures in 2-D in Fig. 19a/b.4. In Fig. 19b.2, the peak shock pressures from the diverging shock wave are distinguished from the peak shock pressures from the converging shock wave (Kozlov and Sazonova 2012).
- The progressive shock metamorphism recorded in the sample is shown in Fig. 19a/b.2 (Stöffler et al. 2018, with C-S4, C-S5, C-S6, the transitions, and C-S7, whole rock melting).

The initial pressure at the rim of the spherical sample is ~25 GPa and rises to pressures above 400 GPa at the centre of the spherical sample due to the converging geometry of the shock wave. When the maximum pressure is reached at the centre of the sample, an outward diverging shock wave causes a secondary rise in shock pressures due to superposition with the inward propagating shock wave (such as observed in spherical shocks, Bezaeva et al. 2010, Kozlov and Sazonova 2012). The diverging shock wave then decays and no reflection occurs at the steel ring interface with the sample.

Shock stages recorded in Fig. 19a.2, before the diverging shock wave occurs, show the following distributions from centre of the sample:

- Whole rock melt, C-S7, spans a band from

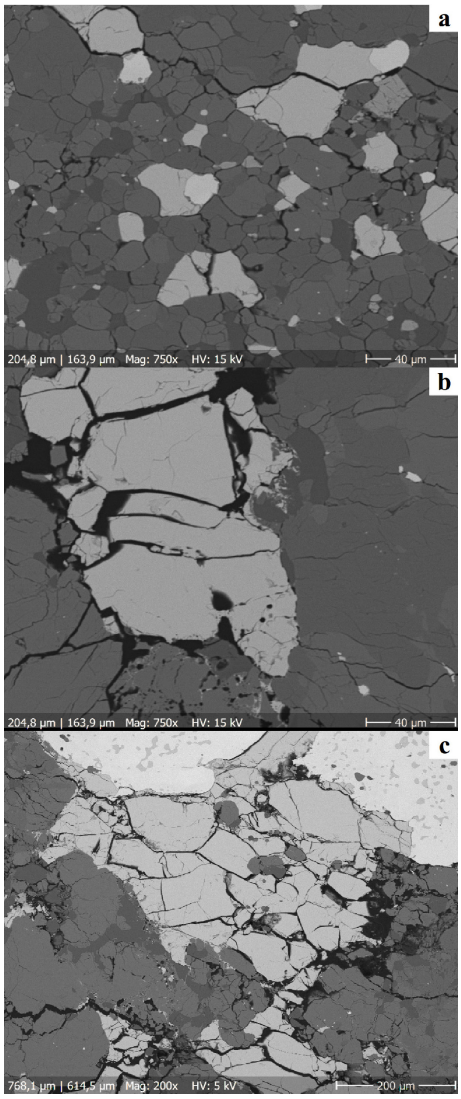

Fig. 18. BSE images of troilite grains in the experimentally shocked Chelyabinsk LL5 chondrite with a) a cluster of unmolten troilite grains, b) a troilite grain with: intermixed melting of troilite and plagioclase and melting at the bottom of the grain, and c) a troilite grain in contact with kamacite with same melting features as in b). Eutectic mixture between troilite and kamacite is visible in c). The first shock wave pulse originated from the top in the experiment.

~0 cm to ~0.6 cm with pressure reaching values >400 GPa at the centre.

– C-S6, and transition from C-S5, spans a band from ~0.6 cm to ~1.0 cm. The band width is reduced once the diverging shock wave progresses (Fig. 19b.2) and complete melting occurs (C-S7); care must be taken with respect to the final distribution of shock stages because of the reverberated diverging shock wave.
– C-S5, and transition from C-S4, span a band from ~1.0 cm to ~1.5 cm.
– C-S4 is recorded from ~1.0 cm to the rim of the sample.

Although the results of the numerical model help to understand the shock distribution in such experiment, care has to be taken with respect to the shock pulse thickness which is important to understand the final distribution of shock stages and the distribution of pressures (Kozlov and Sazonova 2012). Other than this, the model is in good agreement with observations from Kohout et al. (2018) and Petrova et al. (2018) with the following differences:

– C-S4 spans a larger band in Petrova et al. (2018) until 0.9 cm near the centre of the sample. Shock metamorphism in spherically shocked samples is progressive, thus transition from C-S4 to C-S5 may not have been easily observed in the shocked sample and integrated to the numerical modelling results.
– Hence, C-S5 spans a very thin band in Petrova et al. (2018), but corresponding pressure in the model and the spherically shocked sample are similar at the 0.8–0.9 cm distance from the centre (Kohout et al. 2018).
– C-S6 corresponds well to Petrova et al. (2018) until the diverging shock wave occurs. However, no cavity was formed (from melting and vaporization) in Petrova et al. (2018), such as observed in Kozlov and Sazonova (2012), which would have verified the very high shock pressures recorded in Fig. 19.

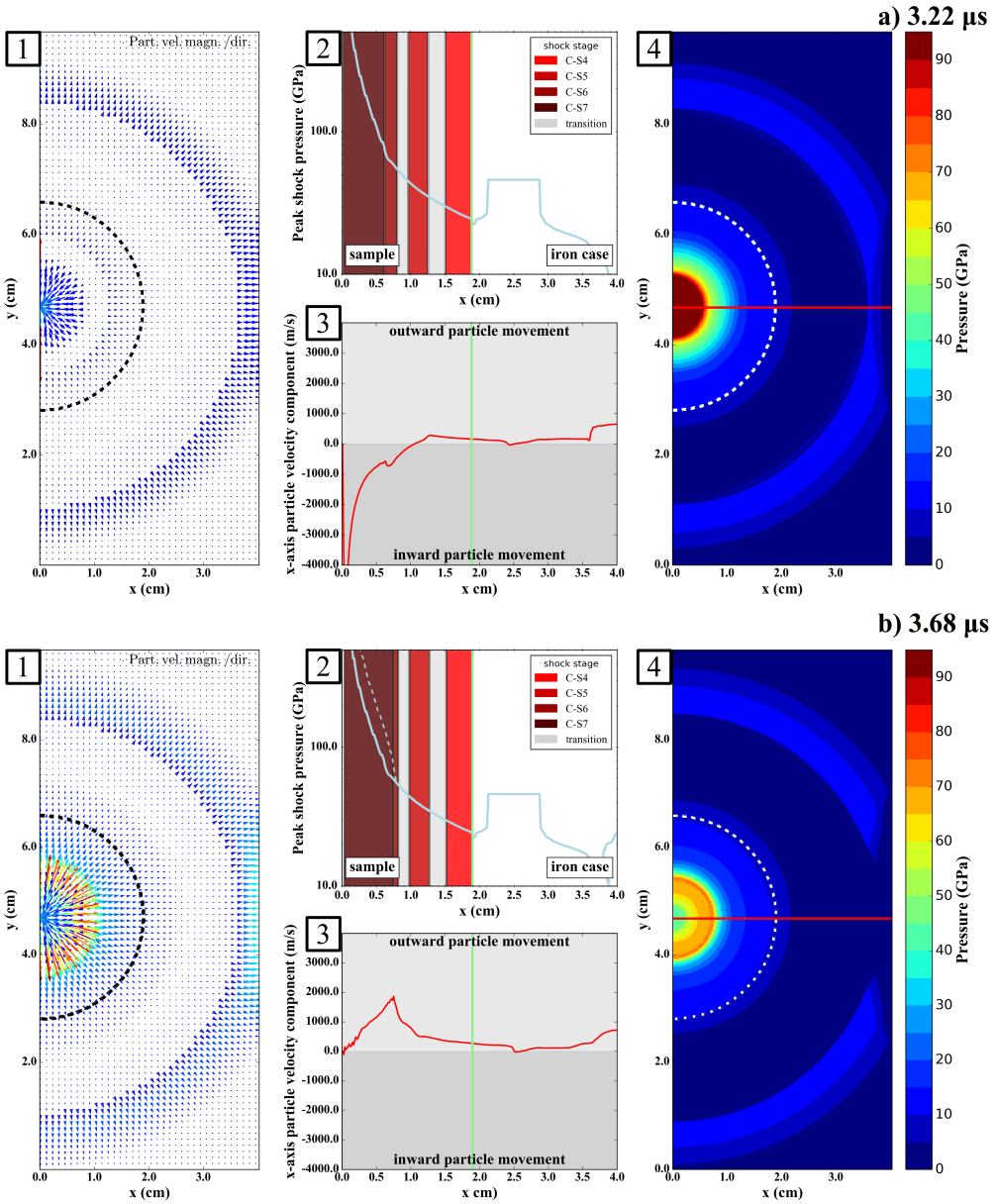

Fig. 19. Numerical results for the spherical shock-recovery experiment model with 1) 2-D particle velocity vectors (with relative magnitudes), 2) cross-sections of peak shock pressures and recorded shock stages, 3) cross-sections of x-axis particle velocity components, 4) 2-D instant pressures; in both a) and b) at time *t* shown in the corner of each graphic. Dashed lines in 2-D projections are demarcations between the spherical olivine sample and the outer iron shell, red lines in 2-D projections are the cross-section locations, green lines in cross-sections are the demarcations for the sample rim. The recorded peak shock pressures from the convergent wave are represented by the plain blue lines in 2), where the dashed line represents the recorded peak shock pressures from the divergent wave in b). The vector magnitudes are specific to a) and b) pressure ranges.

3.6 Asteroid collision simulations

For the simulations, I determined the volumes of material shocked between 40 and 60 GPa for shock-darkening (Paper III) during asteroid collisions. I compared the volumes of shocked material (normalized to the projectile volume, $V_{Shocked}/V_{Proj.}$) as a function of the $R_{Proj.}/R_{Target}$ ratios. The following parameters were used in the study:

- 4, 7, 10 km/s impact velocities with a 0.8 km projectile (0.4 km in radius)
- 0, 15, 30, 50% target porosities
- 30% porosity in the projectile (Britt et al. 2002, between fragmented and rubble-pile asteroid values; Cremonese et al. 2012)
- $R_{Proj.}/R_{Target}$ ratios of 0.5, 0.29, 0.2, 0 (planar impact).

Results are compiled in Fig. 20 and in Table 6 with the given porosities and velocities. At this stage of the study, I can already conclude that the volume of material shocked at 40–60 GPa varies on the impact velocity and the porosity of the target. In the models, volume of shocked material was 3 times the projectile volume for a 10 km/s impact on a nonporous planar target. This value decreased to ~1.5 the volume of the projectile with target porosity of 50%. Less than half of the projectile volume was shocked at 40–60 GPa at 7 km/s impact velocity. At 4 km/s impact velocity and high target porosity (30% and 50%), no material shocked at 40–60 GPa was recorded—the volume of shocked material only attained a value of 0.001 of projectile volume for a nonporous target. Furthermore, all models used a 90º impact angle. Collisions with smaller impact angles produce less volume of shock heated materials (Davison et al. 2014) and, possibly, less volume of material shocked at 40−60 GPa.

At higher $R_{Proj.}/R_{Target}$ ratios, the volume of shocked material in the 10 km/s impact velocity regime is higher for the 15% porous target compared to the nonporous target. Also, from high

Table 6. Numerical results of asteroid collisions

Impact velocity (km/s)	Target porosity[a] (%)	$V_{Shocked}/V_{Proj.}$ [b]	$R_{Proj.}/R_{Target}$ [c]
4	0	0.0006	0.50
4	0	0.0008	0.29
4	0	0.0011	0.20
4	0	0.0006	Planar
7	0	0.2571	0.50
7	0	0.3029	0.29
7	0	0.3209	0.20
7	0	0.3587	Planar
10	0	2.3359	0.50
10	0	2.8045	0.29
10	0	2.8945	0.20
10	0	2.9961	Planar
4	15	0.0001	0.50
4	15	0.0003	0.29
4	15	0.0003	0.20
4	15	0.0000	Planar
7	15	0.2418	0.50
7	15	0.2803	0.29
7	15	0.2956	0.20
7	15	0.3262	Planar
10	15	2.4115	0.50
10	15	2.6829	0.29
10	15	2.7230	0.20
10	15	2.7600	Planar
4	30	0.0000	0.50
4	30	0.0000	0.29
4	30	0.0000	0.20
4	30	0.0000	Planar
7	30	0.2803	0.50
7	30	0.3066	0.29
7	30	0.3149	0.20
7	30	0.3379	Planar
10	30	2.1961	0.50
10	30	2.2948	0.29
10	30	2.3205	0.20
10	30	2.3717	Planar
4	50	0.0000	0.50
4	50	0.0000	0.29
4	50	0.0000	0.20
4	50	0.0000	Planar
7	50	0.0786	0.50
7	50	0.0802	0.29
7	50	0.0802	0.20
7	50	0.0782	Planar
10	50	1.7302	0.50
10	50	1.7202	0.29
10	50	1.7149	0.20
10	50	1.6955	Planar

[a] projectile porosity is 30%
[b] shocked between 40 and 60 GPa
[c] projectile radius is 0.4 km

to low $R_{Proj.}/R_{Target}$ ratios, the progression of volume of shocked material from low to high porosities, in the 10 km/s impact velocity regime, flattens and even has a negative slope for 50% porosity. These observations could be explained by numerical artefacts or the target curvature as briefly explained in section 1.4.3.

As seen in Fig. 21, a planar impact at 10 km/s on a 15% porous target, the crater is a simple crater (low gravity and 0.8 km projectile). The material shocked between 40–60 GPa is situated at the floor and walls of the crater. The model shown in Fig. 21 is not the final crater stage.

4 General discussion and perspectives

4.1 Shock-darkening in experiments

Based on the pressure range of 40–60 GPa for shock-darkening, as determined by the meso-scale models, and the additional results from reverberation and spherical shock-recovery experiment simulations, I can now discuss the outcome of my research and the reliability of such experiments to reproduce shock-darkening.

At first glance, my observations suggest for more shock-recovery experiments at higher pressures in order to reach the required entropy for shock-darkening (no shock-darkening in the shock-recovered Chelyabinsk sample), although higher pressures are difficult to achieve (explosives and experimental set-up).

However, by courtesy of Ralf Schmitt from the Museum für Naturkunde, I could observe, under optical microscope, the Kernouvé H chondrite cold sample (293 K) shocked at 60 GPa (Schmitt 2000). The sample displayed small patches of shock-darkened zones in reflected light, opaque in cross-polarized light, and brown staining of olivine (described by Schmitt 2000) in optically transparent zones. Although the sample was shocked at 60 GPa, shock heating was estimated at ~41 GPa (Schmitt 1995). Using the same experimental set-up from Schmitt (2000), a 2 mm flyer plate, 4 mm steel buffer, 0.5 mm sample with 9% porosity at 293 K initial temperature, I obtained similar results (shock entropy equivalent to a shock of ~39 GPa, see markers in Fig. 14).

With shock-darkening absent in the Chely-

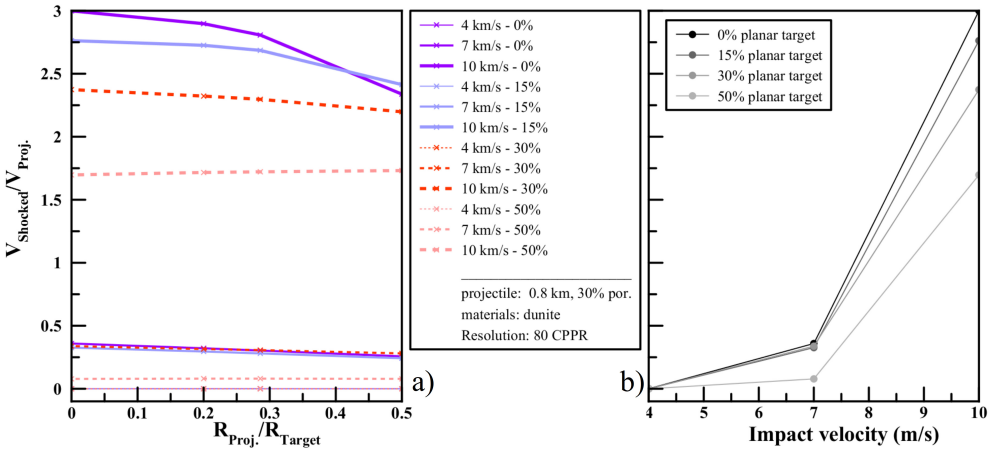

Fig. 20. Volumes of material shocked at 40–60 GPa, normalized to the projectile volume, in simulations of collisions between asteroids. a) all results, at impact velocities and target porosities shown in the legend, of volume of shocked material in function of $R_{Proj.}/R_{Target}$; b) all planar results for volumes of shocked material in function of impact velocity and porosity. Additional information is shown in legend for the projectile size and porosity, materials used for projectile and target, and the simulation resolution (CPPR, cells per projectile radius). Strength properties didn't vary with porosity. $R_{Proj.}/R_{Target}=0$ for planar simulations.

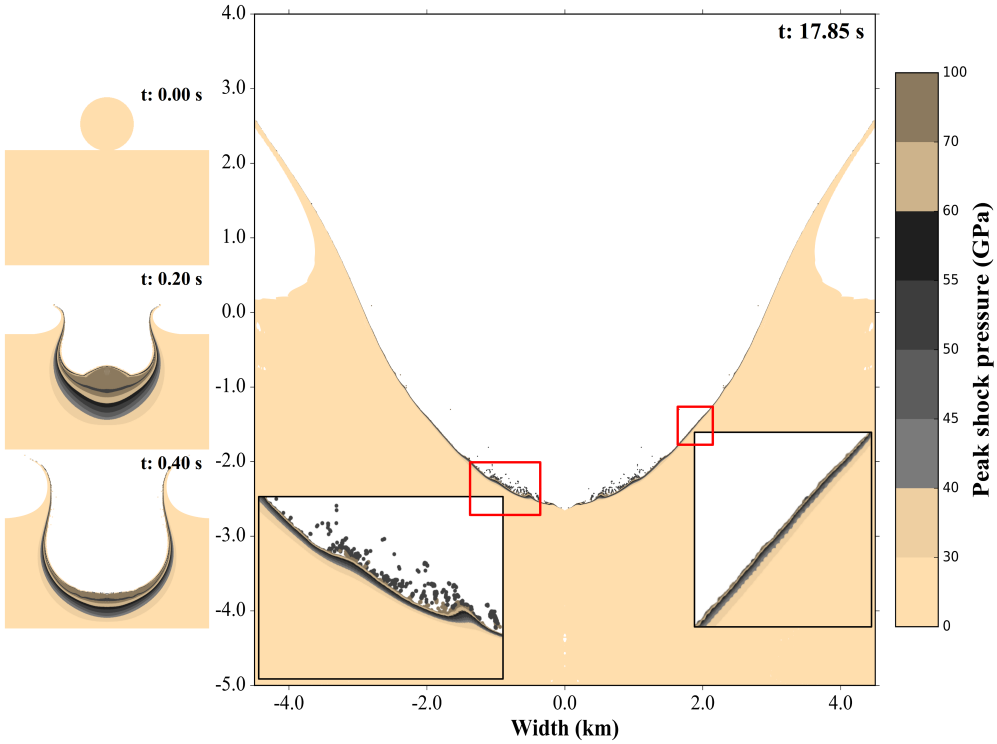

Fig. 21. Positions of material shocked between 40 and 60 GPa from an impact of a 0.8 km dunite projectile into a planar dunite target at 10 km/s at different time step *t*. Porosity of projectile and target were 30% and 15%, respectively. Zones of interest are highlighted for the crater formation at *t*: 17.85 s. Few tracers are visible as single data points and should not be considered as final position for the material.

abinsk LL5 chondrite and small zones of shock-darkening in the Kernouvé H6 chondrite, both experimentally shocked with shock entropy equivalent to 38–41 GPa, I am able to verify my results for the onset of shock-darkening estimated at 40 GPa, although none of these experiments reproduced whole rock shock-darkening.

Furthermore, my results show that spherical shock-recovery experiments are an ideal approach to study shock-darkening. If we can predict the distribution of pressures using numerical models and observations, spherical shock-recovery experiments require less tests to complete a systematic study. Moreover, the spherically shocked sample (Kohout et al. 2018, Petrova et al. 2018), to which experiment I supplied with numerical results in my thesis, features a ring of shock-darkened material at the estimated pressure of ~50 GPa (same location as in Fig. 19a/b.2, the band at 0.8–0.9 cm distance, showing also a 5 GPa rise). Thus, this experiment verifies my results on the estimated pressure range for whole rock shock-darkening (40–60 GPa).

Using either shock-recovery experimental techniques, series of tests on H, L, LL, and enstatite chondrites, should be carried out, although samples suiting spherical shock-recovery experiments are rare and valuable. It should be tested whether shock-darkening is more effective in LL chondrites than in H chondrites, and at which meteorite porosity shock-darkening likely occurs. For example, a spherical shock recovery experiment on a 12% porous H chondrite did not produce whole-rock shock-darkening (Bezaeva et al. 2010), whereas on the 6% porous Chelyabinsk

LL chondrite, whole-rock shock-darkening was observed (Kohout et al. 2018). Indeed, because of porosity, if silicate melting dominates at pressures for shock-darkening (Paper III), spreading of iron sulphide melt into the silicate cracks may not occur—such as observed in Kohout et al. (2018) and Petrova et al. (2018) where silicates start to melt in the zone inner from the shock-darkening zone.

4.2 Heat diffusion

Compiling my results, and finding promising outcomes with shock-recovery experiments, I although never provided results on heat diffusion, briefly discussed in my published work.

Heat diffusion in heterogeneously shock heated materials could act as a heating agent to melt materials nearby hotspots. However, to study heat diffusion from shock heating requires further considerations:

- Is shock heat diffusion more dependent on the phonon or the photon diffusion between metals, iron sulphides and silicates? Only optically transparent phases, such as silicates, can diffuse through photon heat diffusion (Hofmeister et al. 2007). A few works (e.g. Zel'dovich and Raizer 1969) have studied photon heat diffusion at shock fronts, showing that heat can diffuse already at the front of the shock wave (speed of light). Thus, does heat diffusion by photon has to be considered in shock heating if photon heat diffusion occurs ahead of the shock pulse? Or is it diffusion by phonons that dominates?
- If heat diffusion by phonon is considered (e.g. for metals), will it likely happen during shock compression or at unloading and release of the shock pulse? In other words, what process dominates: a lengthy shock pulse with low heat diffusivity materials or a short shock pulse with higher heat diffusivity materials? During asteroid collisions, the material is under shock pressures for a period of time corresponding to the length of the shock pulse, which depends on several parameters such as: the size of the projectile, the impact velocity, or porosity of the target. With diffusivity of 0.3–1 mm^2/s for olivine (Gibert et al. 2005) and 2.5–8 mm^2/s for metals (Monaghan and Quested 2001) at high temperatures, heat may have partially diffused before release of the shock (e.g. for a 10 km/s impact of a 0.8 km projectile on a nonporous planar target, the shock pulse duration is <0.1 s; it will be <1 s for a 8 km projectile).

Early tests succeeded in converting an iSALE output file to calculate the heat diffusivity of materials at a given temperature in post-shock conditions (e.g. iron, Monaghan and Quested 2001; olivine, Gibert et al. 2005). Ignoring or not the conditions of diffusion either at the peak of the shock or post-shock, one could try to transfer the diffusivity data to a heat diffusion code and see how hotspots can heat surrounding materials.

4.3 Shock-darkening in asteroid collisions

The range of pressures for shock-darkening estimated in my work (40–60 GPa) depicts strong shock processes (C-S5 and C-S6). Thus, shock-darkening may involve other mechanisms than just heating and melting. Spreading of the iron sulphide or metal melt is a mechanical process involving opening of cracks and pressure contrasts during compression and decompression, enabling the injection of the molten phases into the silicates, with a preference for iron sulphides such as described in section 1.6.3. Furthermore, as seen in Kohout et al. (2018), shock-darkening happened in a shock experiment where the sample experienced high cooling rates. This suggests that high cooling rate ejected materials during impacts are as likely to be shock-darkened as

buried materials with low cooling rates.

However, as shown in my preliminary impact results, volumes of material shocked between 40 and 60 GPa are very small assuming the average range of impact velocities and asteroid porosities observed in the MAB (see section 1.5.2). Scenarios producing large volumes of material shocked between 40 and 60 GPa are those with high impact velocities on low porosity targets: for example a fragmented asteroid impacting a monolithic asteroid. Interestingly, high impact velocity (10 km/s) and low target porosity (0–15%) values are still in the range of impact velocities and porosities in today's MAB. Also, the average porosity of an asteroid means that porosity can be heterogeneous, such as loose material hosting boulders of low porosity, ideal conditions for shock-darkening (Paper III). Thus, an impact on a highly porous asteroid does not mean that shock darkening will not occur, but it is important to account for less volume of shock-darkened material in such cases.

To estimate the volume of material that was possibly shock-darkened in the MAB, one can use results from numerical modelling (such as presented in my thesis) and merging these with statistics of impact velocities, impact probabilities, and size distribution of asteroids. And because classification of asteroids is based on reflectance spectra from surfaces of asteroids, it is important to understand if shock-darkened material is either excavated and ejected or exposed during asteroid collisions and, from shock-darkening or space weathering, which process is therefore the most prominent.

5 Conclusions

My thesis proved the efficiency of combining numerical models with shock-recovery experimental approaches, which I used to correctly verify my results. Furthermore, by adding simulations for asteroid collisions, I performed a research study that spanned from the millimetre scale to the kilometre scale, with a common thread of shock-darkening and its pressure–temperature conditions. The major findings of my research are:

I. Shock-darkening is dominated by the melting of iron sulphides over metals and silicates in the 40–60 GPa pressure range at low meteorite porosity.
II. Post-shock heating of phases depends on shock wave effects in the shock pulse such as reflections, concentrations, collisions, pore crushing, as well as on impedance contrasts between phases, pre-heating conditions, eutectic mixtures, and silicate porosity.
III. The numerical results, similar to the shock classification at C-S5 and C-S6, argued the relevance of the shock classification with precursor meteorites of higher porosities or under thermal metamorphism.
IV. The reverberation technique, used for shocking meteorite samples, is not ideal to study shock-darkening compared to spherical shock experiments. This is as, in the former, peak shock pressures are not correlated to the shock entropy. These observations allowed me to search for more shock-recovery experiments, either using more appropriate reverberation techniques or spherical shock experiments.
V. In asteroid collisions, ideal conditions for shock-darkening are collisions with high impact velocities (e.g. 10 km/s) on targets with porosities between 0 and 50%. The volumes of potentially shocked-darkened material in such conditions range from 3 to 1.5 times the impactor volume and depend on the internal structure of asteroids.

References

Amsden A. A., Ruppel H. M., and Hirt C. W. 1980. SALE: A simplified ALE computer program for fluid flow at all speeds. Los Alamos, New Mexico: *Los Alamos National Laboratory Report LA-8095*. 101 pp.

Ahrens T. J. 1979. Equations of state of iron sulfide and constraints on the sulfur content of the Earth. *Journal of Geophysical Research*, 84:985–998.

Ahrens T. J., Holland K. G., and Chen G. Q. 1998. Shock temperatures and the melting point of iron. In: *Shock compression of condensed matter*, eds. Schmidt S. C., Dandekar D. P., and Forbes J. W. Woodbury, New York:AIP Press, 133–136.

Alexander C. M. O'D. 2005. From supernovae to planets: The view from meteorites and interplanetary dust particles. In: *Chondrites and the protoplanetary disk*, eds. Krot A. N., Scott E. R. D., and Reipurth B. San Francisco: Astronomical Society of the Pacific Conference Series, 972–1002.

Anderson C. E. 1987. An overview of the theory of hydrocodes. *International Journal of Impact Engineering*, 5:33–59.

Artemieva N. and Ivanov B. 2004. Launch of Martian meteorites in oblique impacts. *Icarus*, 171:84–101.

Asphaug E., Ostro S. J., Hudson R. S., Scheeres D. J., and Benz W. 1998. Disruption of kilometer-sized asteroids by energetic collisions. *Nature*, 393:437–440.

Ben-Dor G., Igra O., and Elperin T. 2000. *Handbook of shock waves*, Academic Press, Massachusetts, United States, 2102 pp.

Bennett M. E. and McSween Jr. H. Y. 1996. Shock features in iron-nickel metal and troilite of L-group ordinary chondrites. *Meteoritics & Planetary Science*, 31:255–264, doi:org/10.1111/j.1945-5100.1996.tb02021.x.

Benson D. J. 1992. Computational methods in Lagrangian and Eulerian hydrocodes. *Computer Methods in Applied Mechanics and Engineering*, 99(2–3), 235 pp.

Benz W., Cameron A. G. W., and Melosh H. J. 1989. The origin of the Moon and the single-impact hypothesis III. *Icarus*, 81:113–131.

Bezaeva N. S., Badjukov D. D., Rochette P., Gattacceca J., Trukhin V. I., Kozlov E. A., and Uehara M. 2010. Experimental shock metamorphism of the L4 ordinary chondrite Saratov induced by spherical shock waves up to 400 GPa. *Meteoritics & Planetary Science*, 45:1007–1020.

Bischoff A., Scott E. R. D., Metzler K., and Goodrich C. A. 2006. Nature and origins of meteoritic breccias. In: *Meteorites and the Early Solar System II*, eds. Lauretta D. S. and McSween Jr. H. Y., University of Arizona Press, 679–712.

Bland P. A., Collins G. S., Davison T. M., Abreu N. M., Ciesla F. J., Muxworthy A. R., and Moore J. 2014. Pressure–temperature evolution of primordial solar system solids during impact-induced compaction. *Nature communications*, 5:5451, doi:10.1038/ncomms6451.

Borg J. P. and Chhabildas L. C. 2011. Three-dimensional dynamic loading simulations of sand. In: *Proceedings of 11th Hypervelocity Impact Symposium*, eds. Schäfer F. and Hiermaier S., Schriftenreihe Forschungsergebnisse aus der Kurzzeitdynamik, vol. 20. Freiburg: Fraunhofer EMI, 111–123.

Bottke W. F. Jr., Nolan M. C., Greenberg R., and Kolvoord R. A. 1994. Velocity distributions among colliding asteroids. *Icarus*, 107:255–268.

Bottke W. F., Cellino A., Paolicchi P., and Binzel R. P. 2002. *Asteroids III*. The University of Arizona Press, USA, 785 pp.

Britt D. T. and Pieters C. M. 1989. Bidirectional reflectance characteristics of black chondrite meteorites. In: *20th Lunar and Planetary Science Conference*. Houston, Texas, pp. 109–110.

Britt D. T., Pieters C. M., Petaev M. I., and Zaslavskaya, N.I. 1989. The Tsarev meteorite - Petrology and bidirectional reflectance spectra of a shock-blackened L chondrite. In: *19th Lunar and Planetary Science Conference*. Houston, Texas, pp. 537–545.

Britt D. T., Yeomans D., Housen K., and Consolmagno G. 2002. Asteroid density, porosity, and structure. In: *Asteroid III*, eds. Bottke W., Cellino A., Paolicchi P., and Binzel R. P., University of Arizona Press, Tuscon, 485–500.

Brown J. M., Ahrens T. J., and Shampine D. L. 1984. Hugoniot data for pyrrhotite and the Earth's core. *Journal of Geophysical Research*, 89:6041–6048.

Brundage A. L. 2013. Implementation of Tillotson Equation of State for hypervelocity impact of metals, geologic materials, and liquids. *Procedia Engineering*, 58:461–470.

Carry B. 2012. Density of asteroids. *Planetary and Space Science*, 73:98–118, doi:10.1016/j.pss.2012.03.009.

Chen, M. and El Goresy, A. 2000. The nature of maskelynite in shocked meteorites: not diaplectic glass but a glass quenched from shock-induced dense melt at high pressures. *Earth and Planetary Science Letters*, 179:489–502, doi:10.1016/S0012-821X(00)00130-8.

Clark B. E., Hapke B., Pieters C., and Britt D. 2002. Asteroid space weathering and regolith evolution. In *Asteroid III*, eds. Bottke W., Cellino A., Paolicchi P., and Binzel R. P., Tucson, Arizona, The University of Arizona Press. pp. 585–599.

Cmíral M., Gerald J. D. F., Faul H. U, and Green D. H. 1998. A close look at dihedral angles and melt geometry in olivine-basalt aggregates: a TEM study. *Contributions to Mineralogy and Petrology*, 130:336−345.

Collins G. S., Melosh H. J., Morgan J. G., and Warner M. R. 2002. Hydrocode simulations of Chicxulub crater collapse and peak-ring formation. *Icarus*, 157:24–33.

Collins G. S., Melosh H. J., and Ivanov, B. A. 2004. Modeling damage and deformation in impact simulations. *Meteoritics & Planetary Science*, 39:217–231.

Collins G. S., Melosh H. J., and Wünnemann K. 2011. Improvements to the ε–α porous compaction model for simulating impacts into high-porosity solar system objects. *International Journal of Impact Engineering*, 38(6):434–439.

Collins G. S., Wünnemann K., Artemieva N., and Pierazzo E. 2013. Numerical modeling of impact processes. In: *Impact Cratering: Processes and Products*, 1st edition, eds. Osinski G. R. and Pierazzo E., 254–270.

Collins G. S., Elbeshausen D., Wünnemann K., Davison T. M., Ivanov B., and Melosh H. J. 2016. *iSALE-Dellen manual: A multi-material, multi-rheology shock physics code for simulating impact phenomena in two and three dimensions*. doi:org/10.6084/m9.figshare.3473690.

Consolmagno G. J., Britt D. T., and Macke R. J. 2009. The significance of meteorite density and porosity. *Chemie der Erde*, 68:1–29.

Crawford D. A., Barnouin-Jha O. S., and Cintala M. J. 2003. Mesoscale computational investigation of shocked heterogeneous materials with application to large impact craters (abstract #4119). *Third International Conference on Large Meteorite Impacts*, Nördlingen, Germany. CD-ROM.

Cremonese G., Martellato E., Marzari F., Kuhrt E., Scholten F., Preusker F., Wünnemann K., Borin P., Massironi M., Simioni E., Ip W., and the OSIRIS team 2012. Hydrocode simulations of the largest crater on asteroid Lutetia. *Planetary and Space Science*, 66:147–154.

Dai C., Hu J., and Tan H. 2009. Hugoniot temperatures and melting of tantalum under shock compression determined by optical pyrometry. *Journal of Applied Physics*, 106:043519, doi:10.1063/1.3204941.

Davison L. 2008. Plane longitudinal shock. In: *Fundamentals of shock wave propagation in solids*. Berlin: Springer-Verlag. pp. 37–62.

Davison T. M., Collins G. S., and Ciesla F. J. 2010, Numerical modelling of heating in porous planetesimal collisions. *Icarus*, 208(1), 468–481.

Davison T. M., Ciesla F. J., and Collins G. S. 2012. Post-impact thermal evolution of porous planetesimals. *Geochimica et Cosmochimica Acta*, 95:252–269.

Davison T. M., Ciesla F. J., Collins G. S., and Elbeshausen D. 2014. The effect of impact obliquity on shock heating in planetesimal collisions. *Meteoritics & Planetary Science*, 49(12):2252–2265.

Davison T. M., Collins G. S., and Bland P. A. 2016. Mesoscale modeling of impact compaction of primitive solar system solids. *Astrophysical Journal*, 821(68), 17 pp, doi:10.3847/0004-637X/821/1/68.

Davison T. M., Derrick J. G., Collins G. S., Bland P. A., Rutherford M. E., Chapman D. J., and Eakins D. E. 2017. Impact-induced compaction of primitive solar system solids: The need for mesoscale modelling and experiments. *Procedia Engineering*, 204:405–412, doi:10.1016/j.proeng.2017.09.801.

Deller J. F., Lowry S. C., Snodgrass C., Price M. C., and Sierks H. 2016. A new approach to modeling impacts on rubble pile asteroid simulants. *Monthly Notices of the Royal Astronomical Society*, 455:3752–3762, doi:10.1093/mnras/stv2584.

DeMeo F. E. and Carry B. 2014. Solar system evolution from compositional mapping of the asteroid belt. *Nature*, 505:629–634.

DeMeo F. E., Binzel R. P., Slivan S. M., and Bus S. J. 2009. Extension of the Bus asteroid taxonomy into the near-infrared. *Icarus*, 202:160–180.

Ehlers E. G. 1972. *The Interpretation of Geological Phase Diagrams, viii*. W.H. Freeman and Co., Ltd., San Francisco, 280 pp.

Fredriksson K. and Keil K. 1964. The iron, magnesium and calcium distribution in coexisting olivine and rhombic pyroxenes in chondrites. *Journal of Geophysical Research*, 69:3487–3515.

French B. M. 1998. *Traces of Catastrophe: A Handbook of Shock-Metamorphic Effects in Terrestrial Meteorite Impact Structures*. Lunar and Planetary Institute, Texas, USA, 132 pp.

Fritz J., Artemieva N., and Greshake A. 2005. Ejection of Martian meteorites. *Meteoritics & Planetary science*, 40(9/10):1393–1411.

Fritz J., Greshake A., and Fernandes V. A. 2017. Revising the shock classification of meteorites. *Meteoritics & Planetary Science*, 52:1216–1232, doi:10.1111/maps.12845.

Fujita T., Kojima H., and Yanai K. 1999. Origin of metal–troilite aggregates in six ordinary chondrites. *Antarctic Meteorite Research*, 12:19–35.

Gaetani G. A., and Grove T. L. 1999. Wetting of mantle olivine by sulfide melt: implications for Re/Os ratios in mantle peridotite and late-stage core formation. *Earth and Planetary Science Letters*, 169:147–163.

Gibert B., Schilling F. R., Gratz K., and Tommasi A. 2005. Thermal diffusivity of olivine single crystals and a dunite at high temperature: evidence for heat transfer by radiation in the upper mantle. *Physics of the Earth and Planetary Interiors*, 151:129–141.

Goltrant O., Cordier P., and Doukhan J.-C. 1991. Planar deformation features in shocked quartz; a transmission electron microscopy investigation. *Earth and Planetary Science Letters*, 106(1–4):103–115, doi:10.1016/0012-821X(91)90066-Q.

Goltrant O., Leroux H., Doukhan J.-C., and Cordier P. 1992. Formation mechanisms of planar deformation features in naturally shocked quartz. *Physics of the Earth and Planetary Interiors*, 74:219–240.

Gratz A. J., Nellis W. J., Christie J. M., Brocious W., Swegle J., and Cordier P. 1992. Shock metamorphism of quartz with initial temperatures -170 to +1000° C. *Physics and Chemistry of Minerals*, 19:267–288.

Güldemeister N., Wünnemann K., Durr N., and Hiermaier S. 2013. Propagation of impact-induced shock waves in porous sandstone using mesoscale modeling. *Meteoritics & Planetary Science*, 48(1):115–133.

Hesse M. A. 2018. Multi-phase melt percolation during core formation (abstract #611). In: *European Planetary Science Congress 2018*, vol. 12, 16–21 September 2018, Berlin, Germany.

Heymann D. 1967. On the origin of hypersthene chondrites: Ages and shock effects of black chondrites. *Icarus* 6:189–221.

Hofmeister, A. M., Pertermann, M., and Branlund, J. M. 2007. Thermal conductivity of the Earth. In: *Treatise in Geophysics*, ed. in chief Schubert G., V. 2 Mineral Physics, ed. Price G. D., Elsevier, The Netherlands, 543–578.

Holsapple K. A. 1993. The scaling of impact processes in planetary sciences. *Annual Review of Earth and Planetary Science*s, 21:333–373.

Housen K. R. and Holsapple K. A. 2003. Impact cratering on porous asteroids. *Icarus*, 163:102.119.

Hutchison R. 2007. *Meteorites: A Petrologic, Chemical and Isotopic Synthesis*, 1st edition, Cambridge Planetary Science series, Cambridge University Press, UK.

Ivanov B. A. 2005. Shock melting of permafrost on Mars: Water ice multiphase equation of state for numerical modeling and its testing (abstract #1232). *38th Lunar and Planetary Science Conference*, Texas, USA, CD-ROM.

Ivanov B. A., Deniem D., and Neukum G. 1997. Implementation of dynamic strength models into 2D hydrocodes: Applications for atmospheric breakup and impact cratering. *International Journal of Impact Engineering*, 20:411–430.

Jaret S. J., Woerner W. R., Philips B. L., Ehm L., Nekvasil H., Wright S. P., and Glotch T. D. 2015. Maskelynite formation via solid-state transformation: Evidence of infrared and X-ray anisotropy. *Journal of Geophysical Research: Planets*, 120:570–587, doi:10.1002/2014JE004764.

Keil K., Jeffrey F. B., and Britt D. T. 1992. Reflection spectra of shocked ordinary chondrites and their relationship to asteroids. *Icarus*, 98:43–53.

Kohout T., Pesonen L. J., Deutsch A., Wünnemann K., Nowka D., Hornemann U., and Heikinheimo E. 2012. Shock experiments in range of 10–45 GPa with small multidomain magnetite in porous targets. *Meteoritics & Planetary Science*, 47:10, 1671–1680.

Kohout T., Gritsevich M., Grokhovsky V. I., Yakokiev G. A., Haloda J., Halodova P., Michallik R. M., Penttilä A., and Muinonen K. 2014. Mineralogy, reflectance spectra, and physical properties of the Chelyabinsk LL5 chondrite— Insight into shock-induced changes in asteroid regoliths. *Icarus*, 228:78–85.

Kohout T., Petrova E. V., Yakovlev G. A., Grokhovsky V. I., Penttilä A., and Maturilli A. 2018. Spherical shock experiments with Chelyabinsk meteorite: reflectance spectra changes with increasing shock (abstract #827). *European Planetary Science Congress 2018*, vol. 12, 16–21 September 2018, Berlin, Germany.

Kozlov E. A. and Sazonova L. V. 2012. Phase transformations of enstatite in spherical shock waves. *Petrology*, 20(4):336–346, doi:10.1134/S0869591112040078.

Kowitz A., Schmitt R., Reimold W. U., and Hornemann Ulrich 2013. The first MEMIN shock recovery experiments at low shock pressure (5–12.5 GPa) with dry, porous sandstone. *Meteoritics & Planetary Science*, 48(1):99–114, doi:10.1111/maps.12030

Langenhorst F. and Hornemann U. 2005. Shock experiments on minerals: Basic physics and techniques. *EMU Notes in Mineralogy*, 7(15):357–387.

Langenhorst F. and Deutsch A., 1994. Shock experiments on pre-heated alpha- and beta-quartz; I, Optical and density data. *Earth and Planetary Science Letters*, 125:407–420.

Lauretta D. S. and McSween H. Y. 2006. *Meteorites and the Early Solar System II*. University of Arizona Press, USA, 942 pp.

Lichtenberg T., Golabek G. J., Dulleond C. P., Schönbächler M., Gerya T. V., and Meyer M. R. 2018. Impact splash chondrule formation during planetesimal recycling. *Icarus*, 302:27–43.

Lide D. R. 2003. *CRC Handbook of Chemistry and Physics*. Boca Raton: CRC Press, USA, 2660 pp.

Liu Z.-L., Cai L.-C., Chen X.-R., and Jing F.-Q. 2008. Molecular dynamics simulations of the melting curve of tantalum under pressure. *Physical review* B77:024103.

Luo B., Wang G., Mo J., Zhang H., Tan F., Zhao J., Liu C., and Sun C. 2014. Verification of conventional equations of state for tantalum under quasi-isentropic compression. *Journal of Applied Physics*, 116:193506, doi:10.1063/1.4902064.

Mare E. R., Tomkins A. G., and Godel B. M. 2014. Restriction of parent body heating by metal–troilite melting: Thermal models for the ordinary chondrites. *Meteoritics & Planetary Science*, 49(4):636–651.

Marsh S. P. 1980. *LASL shock Hugoniot data*. Berkeley, California: The University of California Press, USA, 674 pp.

McEwen A. S. and Bierhaus E. B. 2006. The impor-

tance of secondary cratering to age constraints in planetary surfaces. *Annual Review of Earth and Planetary Sciences*, 34:535–567.

McQueen R. G., Marsh S. P., and Fritz J. N. 1967. Hugoniot equation of state of twelve rocks. *Journal of Geophysical Research* 72(20):4999–5036.

McSween H. Y. Jr., Bennett M. E. III, and Jarosewich E. 1991. The mineralogy of ordinary chondrites and implications for asteroid spectrophotometry. *Icarus*, 90:107–116.

Melosh H. J. 1989. *Impact cratering: A geologic process*. Oxford: Oxford University Press, UK, 253 pp.

Melosh H. J. 2007. A hydrocode equation of state for SiO_2. *Meteoritics & Planetary Science*, 42:2079–2098.

Melosh H. J., Ryan E. V., and Asphaug E. 1992. Dynamic fragmentation in impacts: Hydrocode simulation of laboratory impacts. *Journal of Geophysical Research*, 97(E9):14735–14759.

Michel P., Tanga P., Benz W., and Richardson D. C. 2002. Formation of asteroid families by catastrophic disruption: simulations with fragmentation and gravitational reaccumulation. *Icarus*, 160:10–23.

Michel P, DeMeo F. E., and Bottke W. F. 2015. *Asteroids IV*. The University of Arizona Press, USA, 952 pp.

Mitchell A. C. and Nellis W. J. 1981. Shock compression of aluminium, copper, and tantalum. *Journal of Applied Physics*, 52:3363–3373.

Monaghan J. J. 1988. An introduction to SPH. *Computer Physics Communications*, 48:89–96.

Monaghan B. J. and Quested P. N. 2001. Thermal diffusivity of iron at high temperature in both the liquid and solid states. *ISIJ International*, 41(12):1524–1528.

Morbidelli A., Walsh K. J., O'Brien D. P., Minton D. A. and Bottke W. F. 2015. The dynamical evolution of the asteroid belt. In: *Asteroids IV*, eds. Michel P. et al., pp. 493–507. Univ. of Arizona, Tucson, doi: 10.2458/azu_uapress_9780816532131-ch026.

Norton O. R. 2002. *The Cambridge encyclopedia of meteorites*, Cambridge, United Kingdom, Cambridge University Press, 374 pp.

O'Brien D. P., Sykes M. V., and Tricarico P. 2011. Collision probabilities and impact velocity distributions for Vesta and Ceres (abstract #2665). *42nd Lunar and Planetary Science Conference*, Texas, USA.

Ostertag R. 1983. Shock experiments on feldspar crystals. *Journal of Geophysical Research: Solid Earth*, 88(S01):B364–B376.

Petrova E. V., Grokhovsky V. I., Kohout T., Muftakhetdinova R. F., and Yakovlev G. A. 2018. Spherical shock experiments with Chelyabinsk meteorite: the experiment and textural gradient (abstract #709–1). *European Planetary Science Congress 2018*, vol. 12, 16–21 September 2018, Berlin, Germany,.

Pierazzo E., Vickery A.M., and Melosh H.J. 1997. A reevaluation of impact melt production. *Icarus*, 127:408–423.

Riedel W., Wicklein M., and Thoma K. 2008. Shock properties of conventional and high strength concrete, experimental and mesomechanical analysis *International Journal of Impact Engineering*, 35:155–171, doi:10.1016/j.ijimpeng.2007.02.001.

Rigg P. A., Scharff R. J., and Hixson R. S. 2014. Sound speed measurements in tantalum using the front surface impact technique. *Journal of Physics: Conference Series*, 500:032018, doi:10.1088/1742-6596/500/3/032018.

Righter K., Abell P., Agresti D., Berger E. L., Burton A. S., Delaney J. S., Fries M. D., Gibson E. K., Haba M. K., Harrington R., Herzog G. F., Keller L. P., Locke D., Lindsay F. N., McCoy T. J., Morris R. V., Nagao K., Nakamura-Messenger K., Niles P. B., Nyquist L. E., Park J., Peng Z. X., Shih C. Y., Simon J. I., Swisher C. C., Tappa M. J., Turrin B. D., and Zeigler R. A. 2015. Mineralogy, petrology, chronology, and exposure history of the Chelyabinsk meteorite and parent body. *Meteoritics & Planetary Sciences*, 50:1790–1819.

Rubin A. E. 1992. A shock-metamorphic model for silicate darkening and compositionally variable plagioclase in CK and ordinary chondrites. *Geochimica et Cosmochimica Acta*, 56:1705–1714, doi:10.1016/0016-7037(92)90236-C.

Rubin A. E. 1997. Mineralogy of meteorite groups. *Meteoritics & Planetary Science*, 32:231–247.

Rubin A. E. 2015. Maskelynite in asteroidal, lunar and planetary basaltic meteorites: An indicator of shock pressure during impact ejection from their parent bodies. *Icarus*, 257:221–229, doi:10.1016/j.icarus.2015.05.010.

Rubin A. E., Scott, E. R. D., and Keil, K. 1997. Shock metamorphism of enstatite chondrites. *Geochimica et Cosmochimica Acta*, 61:847–858, doi:10.1016/S0016-7037(96)00364-X.

Rubin A. E., Breen J. P., Wasson J. T., and Pitt D. 2015. Shock effects in the Willamette ungrouped iron meteorite. *Meteoritics & Planetary Science*, 50(12):1984–1994, doi:10.1111/maps.12569.

Schmidt F. F. and Ogden H. R. 1963. *The Engineering properties of tantalum and tantalum alloys*, DMIC Report 189, Battelle Memorial Institute, Ohio, 121 pp.

Schmitt R. T. 1995. Experimentelle und theoretische Untersuchungen zur Stoßwellenmetamorphose von gewöhnlichen Chondriten. Ph. D. Thesis, FB Geowissenschaften, WWU Münster. 187 pp.

Schmitt R.T., 2000. Shock experiments with the H6 chondrites Kernouvé: Pressure calibration of microscopic shock effects. *Meteoritics & Planetary Science*, 35:545–560.

Scott E. R. D., Keil K., and Stöffler D. 1992. Shock

metamorphism of carbonaceous chondrites. *Geochimica et Cosmochimica Acta*, 56(12):4281–4293.

Sharma R. C., and Chang Y. A. 1979. Thermodynamics and phase relationships of transition metal-sulfur systems: Part III. Thermodynamic properties of the Fe-S liquid phase and the calculation of the Fe-S phase diagram. *Metallurgical Transactions B*, 10B:103-108.

Stöffler D., Keil K,. and Edward S. 1991. Shock metamorphism of ordinary chondrites. *Geochimica et Cosmochimica Acta*, 55(12):3845–3867.

Stöffler D., Horneck G., Ott S., Hornemann U., Cockell C. S., Moeller R., Meyer C., de Vera J.-P., Fritz J. and Artemieva N. A. 2007. Experimental evidence for the potential impact ejection of viable microorganisms from Mars and Mars-like planets. *Icarus*, 186:585–588.

Stöffler D., Hamann C., and Metzler K. 2018. Shock metamorphism of planetary silicate rocks and sediments: Proposal for an updated classification system. *Meteoritics & Planetary Science,* 53:5–49, doi:10.1111/maps.12912.

Taioli S., Cazorla C., Gillan M. J., and Alfè D. 2008. Ab-initio melting curve and principal Hugoniot of tantalum. *Journal of Physics: Conference Series*, 121:012010, doi:10.1088/1742-6596/121/1/012010.

Taylor G. J. and Heymann D. 1971. The formation of clear taenite in ordinary chondrites. *Geochimica et Cosmochimica Acta*, 35:175–188.

Taylor G. J., Maggiore P., Scott E. R. D., Rubin A. E., and Keil K. 1987. Original structures, and fragmentation and reassembly histories of asteroids: Evidence from meteorites. *Icarus*, 69:1–13.

Thompson S. L. and Lauson H. S. 1972. Improvements in the chart-D radiation hydrodynamic code III: revised analytical equation of state. *Report SC-RR-710714*, Sandia National Laboratories, Albuquerque, NM, 113 pp.

Tillotson J. H. 1962. Metallic equations of state for hypervelocity impact. *General Atomic Report GA-3216*, General Atomic, San Diego, CA, 141 pp.

Tomkins A. G. 2009. What metal–troilite textures can tell us about post-impact metamorphism in chondrite meteorites. *Meteoritics & Planetary Science*, 44(8):1133–1149.

Tomkins A.G., Weinberg R.F., Schaefer B.F., and Langendam A. 2013. Disequilibrium melting and melt migration driven by impacts: Implications for rapid planetesimal core formation. *Geochimica et Cosmochimica Acta*, 100:41–59, doi:org/10.1016/j.gca.2012.09.044.

Trunin R. F. 2001. *Experimental data on shock compression and adiabatic expansion of condensed matter*. Sarov, Russia: RFNC-VNIIEF, 446 p.

Van Schmus W. R. and Wood J. A. 1967. A chemical–petrologic classification for the chondritic meteorites. *Geochimica et Cosmochimica Acta*, 31:747–765.

Vedder J. D. 1998. Main Belt asteroid collision probabilities and impact velocities. *Icarus*, 131:283:290.

Vedantam K., Bajaj D., Brar N. S., and Hill S. 2006. Johson-Cook Strength Models for Mild and DP 590 Steels. In: *Shock compression of condensed matter, Proceedings of the Conference of the American Physical Society Topical Group on Shock Compression of Condensed Matter*, AIP Conference Proceedings, 845:775–778.

von Bargen N., and Waff H. S. 1986. Permeabilities, interfacial areas and curvatures of partially molten systems: Results of numerical computations of equilibrium microstructures. *Journal of Geophysical Research*, 91(B9):9261–9276.

Walton E. L. and McCarthy S. 2017. Mechanisms of ringwoodite formation in shocked meteorites: Evidence from L5 chondrite Dhofar 1970. *Meteoritics & Planetary Science*, 52(4):762–776, doi:10.1111/maps.12829.

Wang B., Miao B., Wang J., and Zhang J. 2011. Shock effects and the classification of H-chondrites from the Grove Mountains, East Antarctica: Implications for the shock history of H-chondrite parent bodies. *Advances in Polar Science*, 22(2):81–91, doi:10.3724/SP.J.1085.2011.00081.

Weisberg M. K., McCoy T. J., and Krot A. N. 2006. Systematics and evaluation of meteorite classification. In: *Meteorites and the Early Solar System II*, eds. Lauretta D. S. and McSween H. Y., University of Arizona Press, USA, 19–52.

Wilson J. N. 2001. *Design, Testing, and Utilization of a Spherical Shock-recovery System to Investigate Material Response to Ultrahigh Pressure*. Doctoral thesis, Texas Tech University, USA, 122 pp.

Wilson J. 2004. *Sensor technology handbook*, 1st edition, ed. Wilson J., Newnes, Oxford, UK, 704 pp.

Wünnemann K., Collins G., and Melosh H. 2006. A strain-based porosity model for use in hydrocode simulations of impact and implication for transient crater growth in porous targets. *Icarus*, 180:514–527.

Wünnemann K. Collins G. S., and Osinski G. R. 2008. Numerical modelling of impact melt production in porous rocks. *Earth and Planetary Science Letters*, 269:529–538.

Zel'dovich Y. B. and Raizer Y. P. 1969. Shock waves and radiation. *Annual Review of Fluid Mechanics*, 1:385–412.

Zel'dovich Y. B. and Raizer Y. P. 2002. *Physics of shock waves and high-temperature hydrodynamic phenomena*, eds. Hayes W. D. and Probstein R. F., New York: Dover Publications, New York, USA, 944 pp.